

AD-R165 283

ANALYSIS OF AN APERTURE COUPLED MICROSTRIP ANTENNA(U)

1/1

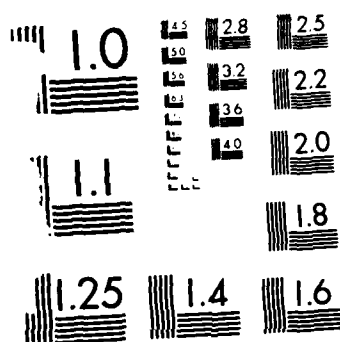
MASSACHUSETTS UNIV AMHERST DEPT OF ELECTRICAL AND
COMPUTER ENGINEERING P L SULLIVAN ET AL. FEB 86
PPG 10 25 871 510632 01 K-2823

UNCLASSIFIED

RADC-TR-85-274 F19628-84-K-0022

F/G 9/5

34



MICROCOPY RESOLUTION TEST CHART
NATIONAL BUREAU OF STANDARDS 1963 A

AD-A165 283

RADC-TR-85-274
Interim Report
February 1986



ANALYSIS OF AN APERTURE COUPLED MICROSTRIP ANTENNA

University of Massachusetts

Peter L. Sullivan
Daniel H. Schaubert

DTIC
SELECTED
S D
MAR 18 1986
D

APPROVED FOR PUBLIC RELEASE; DISTRIBUTION UNLIMITED

ROME AIR DEVELOPMENT CENTER
Air Force Systems Command
Griffiss Air Force Base, NY 13441-5700

This report has been reviewed by the RADC Public Affairs Office (PA) and is releasable to the National Technical Information Service (NTIS). At NTIS it will be releasable to the general public, including foreign nations.

RADC-TR-85-274 has been reviewed and is approved for publication.

APPROVED:



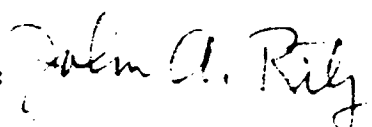
DANIEL T. MCGRATH, Capt, USAF
Project Engineer

APPROVED:



ALLAN C. SCHELL
Chief, Electromagnetic Sciences Division

FOR THE COMMANDER:



JOHN A. RITZ
Plans & Programs Division

DESTRUCTION NOTICE - For classified documents, follow the procedures in DOD 5200.22-M, Industrial Security Manual, Section II-19 or DOD 5200.1-R, Information Security Program Regulation, Chapter IX. For unclassified, limited documents, destroy by any method that will prevent disclosure of contents or reconstruction of the document.

If your address has changed or if you wish to be removed from the RADC mailing list, or if the addressee is no longer employed by your organization, please notify RADC (EEAA) Hanscom AFB MA 01731. This will assist us in maintaining a current mailing list.

Do not return copies of this report unless contractual obligations or notices on a specific document requires that it be returned.

DISCLAIMER NOTICE

**THIS DOCUMENT IS BEST QUALITY
PRACTICABLE. THE COPY FURNISHED
TO DTIC CONTAINED A SIGNIFICANT
NUMBER OF PAGES WHICH DO NOT
REPRODUCE LEGIBLY.**

UNCLASSIFIED

SECURITY CLASSIFICATION OF THIS PAGE

JN-A16.5 283

REPORT DOCUMENTATION PAGE

1a REPORT SECURITY CLASSIFICATION UNCLASSIFIED		1b. RESTRICTIVE MARKINGS N/A	
2a SECURITY CLASSIFICATION AUTHORITY N/A		3. DISTRIBUTION/AVAILABILITY OF REPORT Approved for public release; distribution unlimited	
2b DECLASSIFICATION/DOWNGRADING SCHEDULE N/A			
4. PERFORMING ORGANIZATION REPORT NUMBER(S) N/A		5. MONITORING ORGANIZATION REPORT NUMBER(S) RADC-TR-85-274	
6a. NAME OF PERFORMING ORGANIZATION University of Massachusetts	6b. OFFICE SYMBOL <i>(If applicable)</i> EEAA	7a. NAME OF MONITORING ORGANIZATION Rome Air Development Center (EEAA)	
6c. ADDRESS (City, State, and ZIP Code) Department of Electrical & Computer Engr Amherst MA 01003		7b. ADDRESS (City, State, and ZIP Code) Hanscom AFB MA 01731	
8a. NAME OF FUNDING/SPONSORING ORGANIZATION Rome Air Development Center	8b. OFFICE SYMBOL <i>(If applicable)</i> EEAA	9. PROCUREMENT INSTRUMENT IDENTIFICATION NUMBER F19628-84-K-0022	
10. SOURCE OF FUNDING NUMBERS		PROGRAM ELEMENT NO 61102F	PROJECT NO 2305
		TASK NO J3	WORK UNIT ACCESSION NO. 43
11. TITLE <i>(Include Security Classification)</i> ANALYSIS OF AN APERTURE COUPLED MICROSTRIP ANTENNA			
12. PERSONAL AUTHOR(S) Peter L. Sullivan, Daniel H. Schaubert			
13a. TYPE OF REPORT Interim	13b. TIME COVERED FROM Jan 84 TO Jul 85	14. DATE OF REPORT (Year, Month, Day) February 1986	15. PAGE COUNT 72
16. SUPPLEMENTARY NOTATION N/A			
17. COSATI CODES		18. SUBJECT TERMS <i>(Continue on reverse if necessary and identify by block number)</i> Printed Circuit Antennas Conformal Antennas	
FIELD 17	GROUP 02		
FIELD 09	GROUP 05		
19. ABSTRACT <i>(Continue on reverse if necessary and identify by block number)</i> A new feed configuration for microstrip antennas is analyzed. The antenna consists of a single rectangular microstrip patch coupled through a rectangular aperture to a microstrip line on a separate substrate. The report describes the theory which uses a moment method analysis to calculate the antenna's input impedance. The analysis was verified by comparison with measurements of patch antennas on a low-dielectric-constant substrate (2.54) and the Feed line on high-dielectric-constant (10.2) substrate.			
20. DISTRIBUTION/AVAILABILITY OF ABSTRACT <input type="checkbox"/> UNCLASSIFIED/UNLIMITED <input checked="" type="checkbox"/> SAME AS RPT <input type="checkbox"/> DTIC USERS		21. ABSTRACT SECURITY CLASSIFICATION UNCLASSIFIED	
22a. NAME OF RESPONSIBLE INDIVIDUAL Daniel T. McGrath, Capt, USAF		22b. TELEPHONE <i>(Include Area Code)</i> (617) 861-4036	22c. OFFICE SYMBOL RADC (EEAA)

TABLE OF CONTENTS

<u>Chapter I</u>	
Introduction.....	1
<u>Chapter II</u>	
Theory.....	3
<u>Chapter III</u>	
Results.....	38
<u>Chapter IV</u>	
Conclusion.....	62
<u>References.....</u>	64

Accession For	
NTIS	CRA&I
DTIC	TAB
Unannounced	
Justification _____	
By _____	
Distribution/ _____	
Availability Codes	
Dist	Avail and/or Special
A-1	23

CHAPTER I

INTRODUCTION

A new feed configuration for microstrip antennas has been proposed by Pozar [1]. The feed and a rectangular patch antenna are shown in Figure 2.2. The feed consists of an open ended microstrip line which is located on a dielectric slab below the ground plane. The microstrip antenna is formed on a separate dielectric slab above the ground plane and the two structures are electromagnetically coupled through an electrically small aperture in the ground plane between them.

This design is particularly advantageous when applied to millimeter wave monolithic phased arrays. In this application the associated active elements such as phase shifters and amplifiers would be formed on gallium arsenide, which has a high dielectric constant ($\epsilon_r = 12.8$). However, it is preferable to mount the antenna elements on a low dielectric constant substrate in order to increase the bandwidth, the radiation efficiency and the angle off broadside at which scan blindness occurs [2]. With the bi-layered design, the antennas would be located on a separate substrate which would yield optimal array performance and eliminate the competition for surface space between the antenna elements and the active devices. In addition, the ground plane shields the antenna half space from spurious radiation emitted by the feed lines and active devices. Finally, aperture coupling obviates problems associated

with probe feeds at millimeter wave frequencies, such as complexity of construction and large probe self-reactances [1].

The scope of this thesis is limited to the analysis of a single rectangular microstrip antenna coupled to a microstrip line by a rectangular aperture. The goal of the analysis is to accurately compute the input impedance as a function of frequency, geometry and material parameters. The analysis employs the moment method and the resulting Sommerfeld type integrals are numerically evaluated. Some analytical results are compared to experimental results to verify the theory.

Two approaches are pursued in the calculation of the input impedance. The first approach is to analyze the structure shown in Figure 2.2 directly whereas the second approach involves extending the feed line to infinity in order to calculate the two-port S-parameters of the antenna. In the latter approach the input impedance can be calculated by simple transmission line theory when the feed line is terminated in an open circuit. Although the S-parameter approach is slightly less rigorous than the direct approach, since any interaction between the open circuit termination and the aperture is not taken into account, the effect of any stub length on input impedance can be calculated rapidly once the S-parameters are known.

CHAPTER II

THEORYFormulation of the Problem

A schematic of the antenna and feed line is shown in Figure 2.1 with impressed and scattered currents indicated on the different antenna structures. In order to simplify the analysis the ground plane and dielectric substrates extend to infinity in the \hat{x} - and \hat{y} - directions. The electric surface currents on the patch antenna and feed line and the electric field in the aperture are all assumed to be \hat{y} - directed (see Figure 2.1a). By invoking the equivalence principle the aperture can be closed off and replaced by magnetic surface currents just above and below the ground plane (see Figure 2.1b). The magnetic current above the ground plane is simply the negative of that below, to ensure continuity of the tangential electric field through the aperture.

Denoting the space below the ground plane ($z < 0$) as region a and the space above the ground plane ($z > 0$) as region b the total electric and magnetic fields in each region can be broken into a summation of fields due to the various currents as follows:

$$\bar{E}_a^{\text{tot}} = \bar{E}_a(\bar{J}_{\text{inc}}) + \bar{E}_a(\bar{J}_f) + \bar{E}_a(\bar{M}_s) \quad (1)$$

$$\bar{H}_a^{\text{tot}} = \bar{H}_a(\bar{J}_{\text{inc}}) + \bar{H}_a(\bar{J}_f) + \bar{H}_a(\bar{M}_s) \quad (2)$$

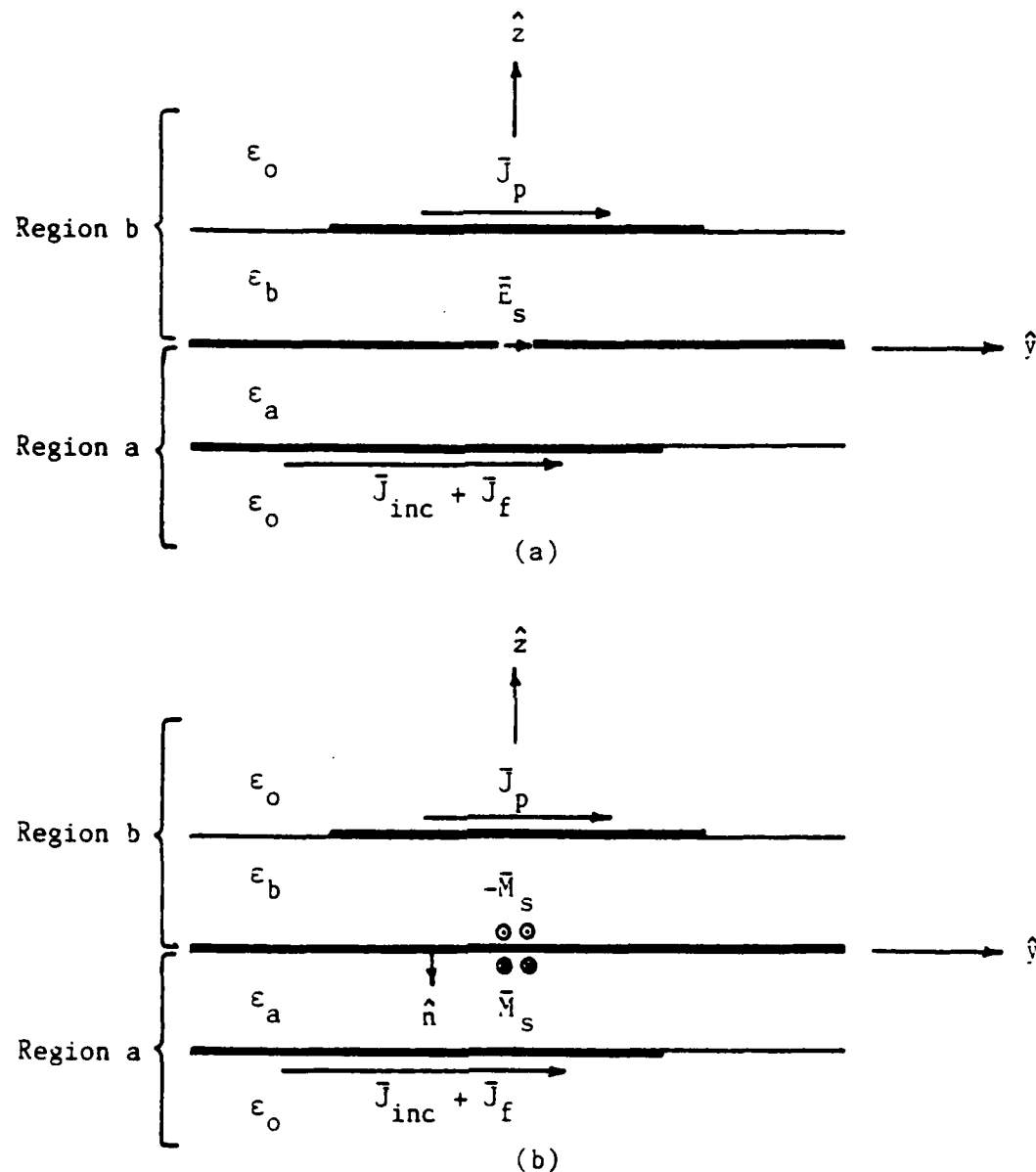


Figure 2.1 Schematic of antenna and feed showing impressed and scattered currents for; (a) original problem, (b) equivalent problem.

$$\bar{E}_b^{\text{tot}} = \bar{E}_b(\bar{J}_p) - \bar{E}_b(\bar{M}_s) \quad (3)$$

$$\bar{H}_b^{\text{tot}} = \bar{H}_b(\bar{J}_p) - \bar{H}_b(\bar{M}_s) \quad (4)$$

Each field on the right hand side of (1)-(4) is the field due to the current specified with the aperture shorted. The unknown scattered electric currents on the feed line and antenna are \bar{J}_f and \bar{J}_p respectively. The unknown magnetic current representing the aperture electric field is \bar{M}_s . In region b the negative sign on \bar{M}_s can be brought outside the parentheses because the field is linearly related to the current.

The first step in the moment method solution of this problem is to expand the unknown currents in a finite set of basis currents of unknown amplitude. The surface current density on the antenna element is expanded in a set of piecewise sinusoidal (PWS) basis functions which vary in the \hat{y} - direction and are constant in the \hat{x} direction as shown in (5)-(9).

$$\bar{J}_p(x, y) = \sum_{l=1}^{N_b} I_l^b \bar{J}_l^b(x, y) \quad (5)$$

where

$$\bar{J}_l^b(x, y) = - \frac{i \sin k_e^b (h^b - |y - y_l|)}{W_p \sin k_e^b h^b} \hat{y}, \quad x_{os} - W_p/2 \leq x \leq x_{os} + W_p/2, \quad y_l - h^b \leq y \leq y_l + h^b \quad (6)$$

$$k_e^b = (\epsilon_{re}^b)^{1/2} k_0 \quad (7)$$

$$\epsilon_{re}^b = (\epsilon_r^b + 1)/2 + ((\epsilon_r^b - 1)/2)(1 + 10d_b/W_p)^{-1/2} \quad (8)$$

$$h^b = L_p / (N_b + 1) \quad (9)$$

I_1^b is the unknown coefficient corresponding to the 1th PWS basis function, J_1^b . The effective dielectric constant, ϵ_{re}^b is taken from Carver and Mink [3]. The patch length, i.e., the resonant length dimension, and width are given by L_p and W_p respectively. The lateral offset of the patch in the \hat{x} -direction is x_{os} and the antenna dielectric substrate thickness is d_b (see Figure 2.2). The mode half width is h_b (see Figure 2.3 a).

Because the aperture is assumed electrically short the magnetic current can be represented by only a single PWS current mode. Noting that the aperture is always centered about the origin in Figure 2.2, this current can be written as

$$\bar{M}_s(x, y) = V_{ap}^{ap} \bar{M}^{ap}(x, y) \quad (10)$$

where

$$V_{ap}^{ap} = -V_o \quad (11)$$

$$\bar{M}^{ap}(x, y) = \frac{1}{W_{ap}} \frac{\sin k_{ap} (L_{ap}/2 - |x|)}{\sin k_{ap} L_{ap}/2} x, \quad \begin{aligned} -L_{ap}/2 &< x < L_{ap}/2 \\ -W_{ap}/2 &< y < W_{ap}/2 \end{aligned} \quad (12)$$

$$k_{ap} \leq \pi/L_{ap} \quad (13)$$

V_o is the unknown voltage across the center of the aperture. The aperture length, i.e., the long dimension, is L_{ap} and the width is W_{ap} (see Figure 2.2). The parameter k_{ap} must be determined by comparison of analytical to empirical results, since its value can vary the aperture distribution from essentially triangular to cosinusoidal. It will be

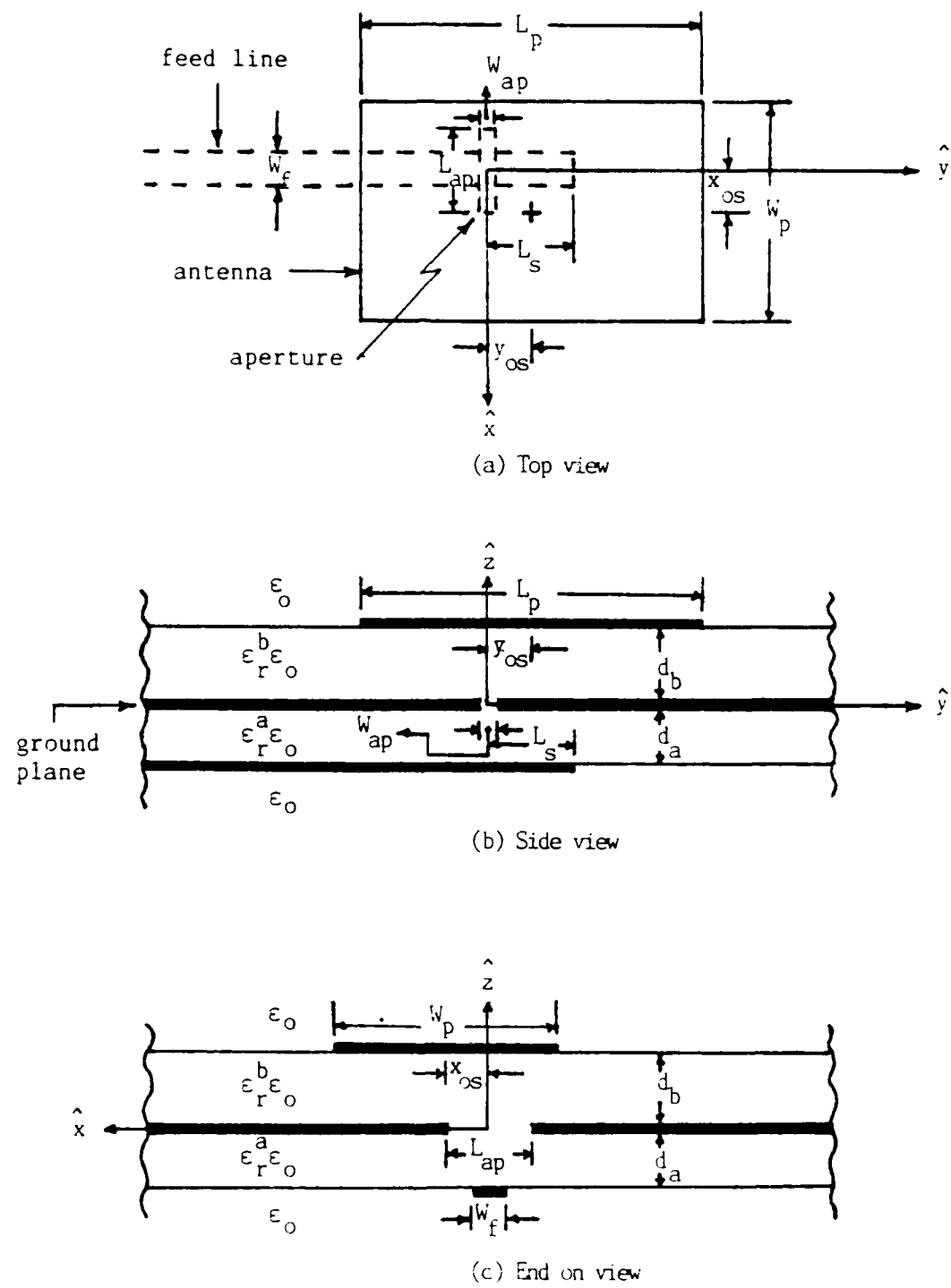


Figure 2.2 Schematic of antenna and feed which defines all material and architectural parameters and the orientation of various structures with respect to the coordinate system.

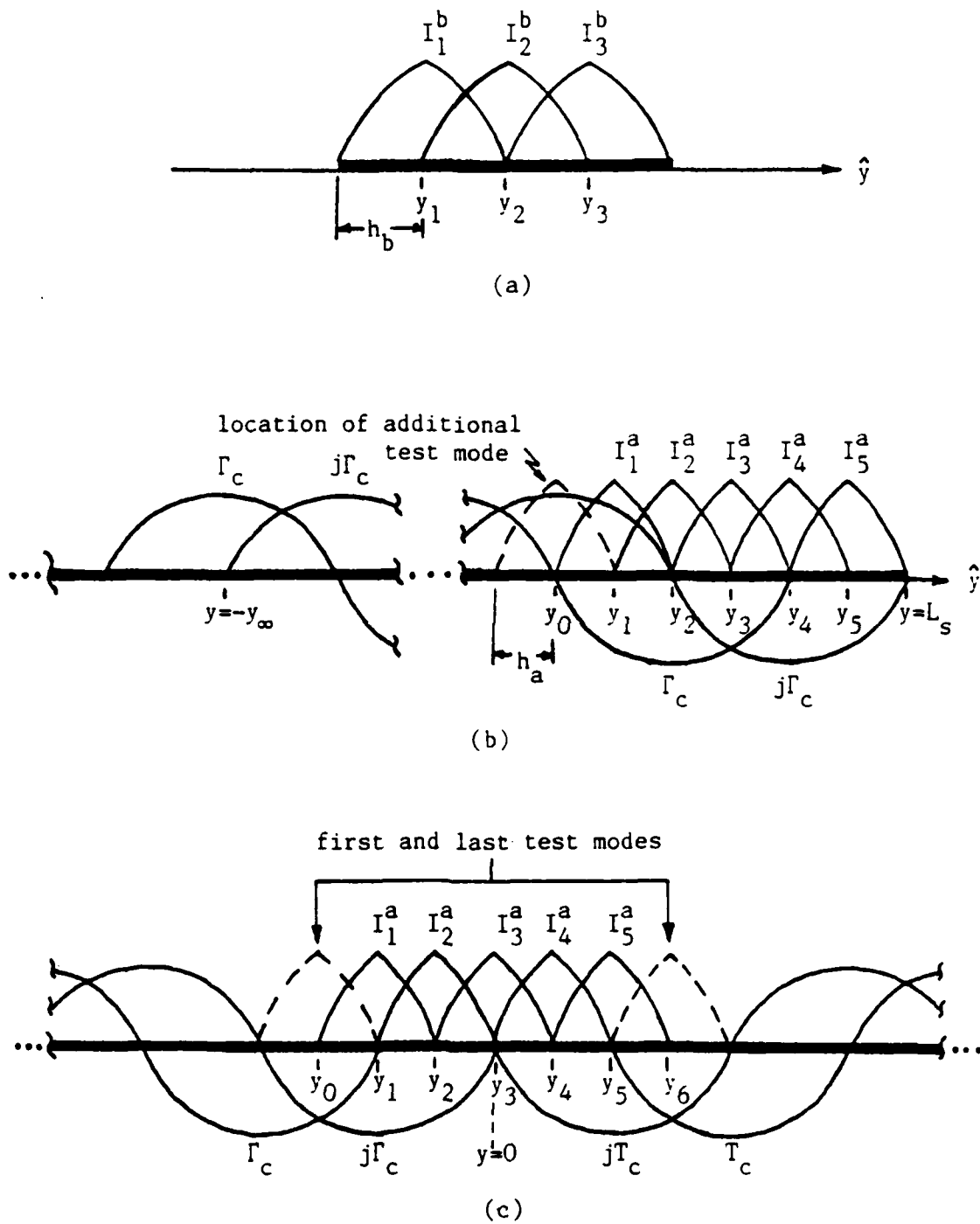


Figure 2.3 Layout of basis modes and those test modes which do not correspond to any basis modes on the (a) antenna element, (b) semi-infinite feed line terminated in an open, (c) infinite feed line.

seen later that a general expression for k_{ap} can be found, which is a function of the material parameters and antenna geometry and yields good agreement between measured and calculated results in all cases studied.

The current on the feed line is expanded in a combination of subsectional and entire domain basis functions. The incident and reflected currents are represented by traveling wave modes corresponding to the fundamental microstrip mode over the entire feed line. The total traveling wave surface current is then

$$\bar{J}'_{trav}(x,y) = \bar{J}'_{inc}(x,y) + \bar{J}'_{ref}(x,y) \quad (14)$$

where

$$\bar{J}'_{inc}(x,y) = \frac{1}{W_f} e^{-jk_e^a(y-L_s)} \hat{y}, \quad -W_f/2 \leq x \leq W_f/2, \quad y \leq L_s \quad (15)$$

$$\bar{J}'_{ref}(x,y) = \Gamma_c \frac{1}{W_f} e^{jk_e^a(y-L_s)} \hat{y}, \quad -W_f/2 \leq x \leq W_f/2, \quad y \leq L_s \quad (16)$$

The current reflection coefficient, referenced to the end of the line, is Γ_c . The length of feed line from the center of the aperture to the open circuited termination is L_s and the feed line width is W_f (see Figure 2.2). The term k_e^a is the exact propagation constant of the fundamental microstrip mode. It is calculated in a manner outlined by Jackson and Pozar [3].

Writing \bar{J}'_{trav} in terms of real functions, in order to facilitate the numerical evaluation of subsequent integrals, yields

$$\bar{J}'_{trav}(x,y) = (\Gamma_c + 1) \frac{1}{W_f} \cos k_e^a (y - L_s) \hat{y} + j(\Gamma_c - 1) \frac{1}{W_f} \sin k_e^a (y - L_s) \hat{y} \quad (17)$$

The cosine term in (17) violates the boundary condition on the current at an open in all cases except Γ_c equal to -1. To allow for general solutions for Γ_c , the cosine term is truncated $\lambda_f/4$ (λ_f denotes guide wavelengths) from the open ended termination. This is shown schematically in Figure 2.3b. With this condition imposed the incident and reflected currents are altered near the end of the line and are given by

$$\bar{J}_{inc}(x,y) = \bar{J}_c^a(x,y) - j\bar{J}_s^a(x,y) \quad (18)$$

$$\bar{J}_{ref}(x,y) = \Gamma_c(\bar{J}_c^a(x,y) + j\bar{J}_s^a(x,y)) \quad (19)$$

where

$$\bar{J}_c^a(x,y) = \frac{1}{W_f} \cos k_e^a (y - L_s) \hat{y}, \quad \begin{matrix} -W_f/2 < x < W_f/2 \\ -(y_\infty + \pi/(2k_e^a)) < y < L_s - \pi/(2k_e^a) \end{matrix} \quad (20)$$

$$\bar{J}_s^a(x,y) = \frac{1}{W_f} \sin k_e^a (y - L_s) \hat{y}, \quad \begin{matrix} -W_f/2 < x < W_f/2 \\ -y_\infty < y < L_s \end{matrix} \quad (21)$$

From (20) and (21), it can be seen that the traveling wave current mode is finite in length. A semi-infinite traveling wave current mode could be used, but this introduces an additional pole in the integrands which contain this mode. Complexities associated with treating this pole as well as convergence problems are avoided by truncating the traveling wave current mode in the above manner. The semi-infinite line is approximated by making the traveling wave mode a few free space

wavelengths long and by employing an appropriate testing procedure to be described later.

In the vicinity of the aperture and open circuited termination, PWS basis functions are used to represent non-traveling wave currents which arise due to these discontinuities. Thus, the total scattered current on the feed line is

$$\bar{J}_f(x, y) = \sum_{n=1}^N I_n \bar{J}_n^a(x, y) + \Gamma_c(\bar{J}_c^a(x, y) + j\bar{J}_s^a(x, y)) \quad (22)$$

where

$$\bar{J}_n^a(x, y) = -\frac{1}{W_f} \frac{\sin k_e^a (h_a^a - |y - y_n|)}{\sin k_e^a h_a^a} y, \quad -W_f/2 \leq x \leq W_f/2 \quad (23)$$

$$h_a^a = (L_s - y_o) / (N_a + 1) \quad (24)$$

I_n^a is the amplitude coefficient of the n^{th} PWS current mode, \bar{J}_n^a . The microstrip feed width is W_f . Parameters h_a^a and y_o are respectively the PWS mode half width and the y coordinate of the left edge the first ($n=1$) PWS basis mode (see Figure 2.3b).

Substituting the expressions for \bar{J}_p , \bar{M}_s , \bar{J}_{inc} , and \bar{J}_f given in (5), (10), (18) and (22) respectively into (1)-(4) and utilizing the properties of linear operators yields

$$\begin{aligned} \bar{E}_a^{\text{tot}} = & \bar{E}_a(\bar{J}_c^a) - j\bar{E}_a(\bar{J}_s^a) + \sum_{n=1}^N I_n^a \bar{E}_a(\bar{J}_n^a) \\ & + \Gamma_c [\bar{E}_a(\bar{J}_c^a) + j\bar{E}_a(\bar{J}_s^a)] + V^{\text{ap}} \bar{E}_a(\bar{M}_s^{\text{ap}}) \end{aligned} \quad (25)$$

$$\bar{H}_a^{\text{tot}} = \bar{H}_a(\bar{J}_c^a) - j\bar{H}_a(\bar{J}_s^a) + \sum_{n=1}^N I_n^a \bar{H}_a(\bar{J}_n^a) \quad (26)$$

$$+ r_c [\bar{H}_a(\bar{J}_c^a) + j\bar{H}_a(\bar{J}_s^a)] + v^{\text{ap}} \bar{H}_a(\bar{M}^{\text{ap}})$$

$$\bar{E}_b^{\text{tot}} = \sum_{l=1}^N I_l^b \bar{E}_b(\bar{J}_l^b) - v^{\text{ap}} \bar{E}_b(\bar{M}^{\text{ap}}) \quad (27)$$

$$\bar{H}_b^{\text{tot}} = \sum_{l=1}^N I_l^b \bar{H}_b(\bar{J}_l^b) - v^{\text{ap}} \bar{H}_b(\bar{M}^{\text{ap}}) \quad (28)$$

The individual field components on the right hand side of (25)-(28) represent the fields due to the basis current indicated (\bar{J}_1^b , \bar{M}^{ap} , \bar{J}_c^a , \bar{J}_s^a , and \bar{J}_n^a defined in (6), (12), (20), (21) and (23) respectively) in the presence of the grounded dielectric slab only. To find the unknown current amplitudes which occur in the presence of the antenna, aperture and feed, three boundary conditions must be satisfied. These are zero tangential electric fields on the patch and feed line and continuity of the tangential magnetic field through the aperture. Continuity of the tangential electric field through the aperture has already been imposed by the negative relationship between the magnetic currents above and below the ground plane. These three boundary conditions yield three equations to solve for the three unknown currents \bar{J}_p , \bar{M}_s and \bar{J}_f .

Setting the tangential components of \bar{E}_a^{tot} equal to zero on the feed line yields

$$\left\{ - \sum_{n=1}^N I_n^a \bar{E}_a^t(\bar{J}_n^a) - r_c [\bar{E}_a^t(\bar{J}_c^a) + j\bar{E}_a^t(\bar{J}_s^a)] - v^{\text{ap}} \bar{E}_a^t(\bar{M}^{\text{ap}}) \right. \\ \left. - \bar{E}_a^t(\bar{J}_c^a) - j\bar{E}_a^t(\bar{J}_s^a) \right\} \text{on feed line} \quad (29)$$

where the superscript t indicates tangential components. Equating tangential components of \bar{H}_a^{tot} and \bar{H}_b^{tot} in the aperture gives

$$\left\{ - \sum_{n=1}^N I_n^a \bar{H}_a^t(\bar{J}_n^a) - r_c [\bar{H}_a^t(\bar{J}_c^a) + j \bar{H}_a^t(\bar{J}_s^a)] - v^{ap} [\bar{H}_a^t(\bar{M}_a^{ap}) + \bar{H}_b^t(\bar{M}_s^{ap})] \right. \\ \left. + \sum_{l=1}^N I_l^b \bar{H}_b^t(\bar{J}_l^b) = \bar{H}_a^t(\bar{J}_c^a) - j \bar{H}_a^t(\bar{J}_s^a) \right\} \text{in aperture} \quad (30)$$

and forcing the tangential components of \bar{E}_b^{tot} to zero on the antenna gives the expression below.

$$\left\{ - \sum_{l=1}^N I_l^b \bar{E}_b^t(\bar{J}_l^b) + v^{ap} \bar{E}_b^t(\bar{M}_a^{ap}) = 0 \right\} \text{on antenna} \quad (31)$$

A testing procedure is employed in order to solve for the N , i.e., $N = N_a + N_b + 2$, unknown coefficients such that (29)-(31) are satisfied. Each equation is satisfied in a least mean square sense by dotting it with an appropriate testing function and integrating over the structure where the boundary condition is to be enforced. A Galerkin testing procedure is utilized to enforce the boundary conditions at the antenna and aperture to produce $N_b + 1$ equations. The remaining $N_a + 1$ equations are obtained by testing with all PWS functions on the feed line in the neighborhood of the aperture and open termination. As a result there is one more PWS test function (dashed PWS mode shown in Figure 2.3b) than basis mode. This scheme enforces the boundary condition near the terminated end of the line only, however outside this

region the scattered basis current assumes the form of the fundamental quasi-TEM microstrip mode which automatically satisfies the boundary condition on the feed line. Furthermore, by testing with this procedure the opposite end of the traveling wave mode is not "seen" by the test modes provided the traveling wave mode is terminated relatively far from the aperture $(2-3\lambda_0)$. In this way a good approximation to the infinite line is obtained without convergence problems.

Using the following notation to denote an inner product

$$\langle F, G \rangle_s = \iint_s \bar{F} \cdot \bar{G} \, ds \quad (32)$$

and taking advantage of the linearity of the inner product, (29)-(31) upon testing become respectively

$$\begin{aligned} & - \sum_{n=1}^{N_a} I_n^a \langle \hat{J}_m^a, E_a^y(J_n^a) \rangle_f - \Gamma_c [\langle \hat{J}_m^a, E_a^y(J_c^a) \rangle_f + j \langle \hat{J}_m^a, E_a^y(J_s^a) \rangle_f] \\ & - v^{ap} \langle \hat{J}_m^a, E_a^y(M^{ap}) \rangle_f = \langle \hat{J}_m^a, E_a^y(J_c^a) \rangle_f - j \langle \hat{J}_m^a, E_a^y(J_s^a) \rangle_f, \quad m=0,1,2,\dots,N_a \end{aligned} \quad (33)$$

$$\begin{aligned} & - \sum_{n=1}^{N_a} I_n^a \langle \hat{M}^{ap}, H_a^x(J_n^a) \rangle_{ap} - \Gamma_c [\langle \hat{M}^{ap}, H_a^x(J_c^a) \rangle_{ap} + j \langle \hat{M}^{ap}, H_a^x(J_s^a) \rangle_{ap}] \\ & - v^{ap} [\langle \hat{M}^{ap}, H_a^x(M^{ap}) \rangle_{ap} + \langle \hat{M}^{ap}, H_b^x(M^{ap}) \rangle_{ap}] + \sum_{l=1}^{N_b} I_l^b \langle \hat{M}^{ap}, H_b^x(J_l^b) \rangle_{ap} \\ & = \langle \hat{M}^{ap}, H_a^x(J_c^a) \rangle_{ap} - j \langle \hat{M}^{ap}, H_a^x(J_s^a) \rangle_{ap} \end{aligned} \quad (34)$$

$$- \sum_{l=1}^{N_b} I_l^b \langle \hat{J}_k^b, E_b^y(J_l^b) \rangle_p + v^{ap} \langle \hat{J}_k^b, E_b^y(M^{ap}) \rangle_p = 0, \quad k=1,2,\dots,N_b \quad (35)$$

The superscript x or y on the field quantities indicate which of the two tangential components are selected as a result of dotting the field against the test function. The caret (^) above a current quantity denotes the testing function. The letter(s) cited after each inner product indicates the surface (f=feed, ap=aperture, p=patch) over which the integration is carried out. Equations (33)-(35) can be written in matrix form as follows:

$$[Z^a][I^a] + ([Z^c] + j[Z^s])\Gamma_c - [T^a]V^{ap} = -[Z^c] + j[Z^s] \quad (36)$$

$$-[C^a][I^a] - (c^c + jc^s)\Gamma_c + (y^a + y^b)V^{ap} + [C^b][I^b] = c^c - jc^s \quad (37)$$

$$[Z^b][I^b] + [T^b]V^{ap} = 0 \quad (38)$$

The matrix and vector elements and scalars are defined as follows:

$$z_{mn}^a = \langle -\hat{J}_m^a, E_a^y(J_n^a) \rangle_f \quad N_a+1 \times N_a \quad \text{matrix} \quad (39)$$

$$z_m^c = \langle -\hat{J}_m^a, E_a^y(J_c^a) \rangle_f \quad N_a+1 \times 1 \quad \text{column vector} \quad (40)$$

$$z_m^s = \langle -\hat{J}_m^a, E_a^y(J_s^a) \rangle_f \quad N_a+1 \times 1 \quad \text{column vector} \quad (41)$$

$$z_{kl}^b = \langle -\hat{J}_k^b, E_b^y(J_l^b) \rangle_p \quad N_b \times N_b \quad \text{matrix} \quad (42)$$

$$y^a = \langle -\hat{M}^{ap}, H_a^x(M^{ap}) \rangle_{ap} \quad \text{scalar} \quad (43)$$

$$y^b = \langle -\hat{M}^{ap}, H_b^x(M^{ap}) \rangle_{ap} \quad \text{scalar} \quad (44)$$

$$c_n^a = \langle \hat{M}^{ap}, H_a^x(J_n^a) \rangle_{ap} \quad 1 \times N_a \quad \text{row vector} \quad (45)$$

$$c^c = \langle \hat{M}^{ap}, H_a^x(J_c^a) \rangle_{ap} \quad \text{scalar} \quad (46)$$

$$c^s = \langle \hat{M}^{ap}, H_a^x(J_s^a) \rangle_{ap} \quad \text{scalar} \quad (47)$$

$$c_1^b = \langle \hat{M}^{ap}, H_b^x(J_1^b) \rangle_{ap} \quad 1 \times N_b \quad \text{row vector} \quad (48)$$

$$t_m^a = \langle \hat{J}_m^a, E_a^y(M^{ap}) \rangle_f \quad N_a+1 \times 1 \quad \text{column vector} \quad (49)$$

$$t_k^b = \langle \hat{J}_k^b, E_b^y(M^{ap}) \rangle_p \quad N_a \times 1 \quad \text{column vector} \quad (50)$$

$$I_n^a = I_1^a, I_2^a, \dots, I_{N_a}^a \quad N_a \times 1 \quad \text{column vector} \quad (51)$$

$$I_l^b = I_1^b, I_2^b, \dots, I_{N_b}^b \quad N_b \times 1 \quad \text{column vector} \quad (52)$$

$$m = 0, 1, 2, \dots, N_a \quad n = 1, 2, \dots, N_a$$

$$k = 1, 2, \dots, N_b \quad l = 1, 2, \dots, N_b$$

It is convenient to consolidate some of the quantities above into the new matrices, vectors, and scalars given below.

$$[z_{tot}^a] = [z_{mn}^a \mid (z_m^c + jz_m^s)] \quad N_a+1 \times N_a+1 \quad \text{matrix} \quad (53)$$

$$[c_{tot}^a] = [c_n^a \mid (c^c_j c^s)] \quad 1 \times N_a+1 \quad \text{row vector} \quad (54)$$

$$[I_{tot}^a] = [I_n^a \mid r_c] \quad N_a+1 \times 1 \quad \text{column vector} \quad (55)$$

$$I_{inc} = c^c - j c^s \quad \text{scalar} \quad (56)$$

$$[V_{inc}] = [-z_m^c + jz_m^s] \quad N_a+1 \times 1 \quad \text{column vector} \quad (57)$$

The matrix $[z_{tot}^a]$ represents the impedance matrix for an open ended microstrip line by itself. Likewise, $[z^b]$ is the impedance matrix for a microstrip patch alone. The quantities y^a and y^b are the aperture admittances looking into region a and region b respectively of a slot in a ground plane with dielectric slabs on each side. The vectors $[c_{tot}^a]$ and $[T^a]$ are interaction vectors representing the coupling between the feed line and aperture. Coupling between the antenna and aperture is

contained in $[C^b]$ and $[T^b]$. From reciprocity it can be seen that the elements of the T matrices are related to the C matrices by

$$t_k^b = -c_1^b, \quad k = 1 = 1, 2, \dots, N_b \quad (58)$$

$$t_m^a = -c_n^a, \quad m = n = 1, 2, \dots, N_a \quad (59)$$

In (59) the t_m^a element is actually the $(m+1)^{th}$ element in the vector $[T^a]$ because of the numbering convention given in (33), i.e., m runs from 0 to N_a , whereas all other indices run from 1 to N_a or N_b .

Substituting (53)-(57) into (36)-(38) and solving yields

$$v^{ap} = \frac{I_{inc} + [C_{tot}^a][Z_{tot}^a]^{-1}[v_{inc}]}{y^a + y^b - [C^b][Z^b]^{-1}[T^b] - [C_{tot}^a][Z_{tot}^a]^{-1}[T^a]} \quad (60)$$

$$[I_{tot}^a] = [Z_{tot}^a]^{-1}([v_{inc}] + [T^a]v^{ap}) \quad (61)$$

$$[I_{tot}^b] = -[Z^b]^{-1}[T^b]v^{ap} \quad (62)$$

It should be noted that v_o equals $-v^{ap}$ from (11) and that Γ_c is the bottom element in $[I_{tot}^a]$.

Input Impedance and S-Parameter Analysis

The input impedance referenced to the center of the aperture is easily determined from the current reflection coefficient, Γ_c , by

$$Z_{in} = Z_c \frac{1 - \Gamma_c e^{-j2k_e^a L_s}}{1 + \Gamma_c e^{-j2k_e^a L_s}} \quad (63)$$

where Z_c is the characteristic impedance of the line and L_s is the length of open circuited transmission line beyond the center of the aperture.

It is also of interest to calculate the S-parameters of the aperture backed by the patch antenna. This can be done with only a small modification to the previous analysis. The feed line is extended to infinity in both directions from the aperture. The total traveling wave current now becomes the sum of incident, reflected and transmitted wave components shown in (64).

$$\bar{J}_{trav}^a(x, y) = \bar{J}_{inc}(x, y) + \bar{J}_{ref}(x, y) + \bar{J}_{tran}(x, y) \quad (64)$$

\bar{J}_{inc} and \bar{J}_{ref} are defined as before in (18)-(21) where L_s is set equal to zero. \bar{J}_{tran} is given by

$$\bar{J}_{tran}(x, y) = T_c [\bar{J}_c(x, -y) + j\bar{J}_s(x, -y)] \quad (65)$$

where \bar{J}_c and \bar{J}_s are defined in (20) and (21) with L_s equal to zero and T_c is the current transmission coefficient. The layout of the basis modes for the S-parameter analysis is shown in Figure 2.3c. The modes

are symmetric about the aperture center. The number of unknowns on the feed line now equals $N_a + 2$. $N_a + 2$ equations are obtained by testing with all PWS functions in the vicinity of the aperture. The test PWS functions start a half mode length to the left of the first expansion mode and extend a half mode length to the right of the last expansion mode (see Figure 2.3c). The cosine terms have been truncated a quarter of a wavelength from the aperture to avoid a current discontinuity at that point.

It is evident from the symmetry of the basis currents that the matrix elements representing the coupling of the PWS test modes to the transmitted traveling wave current are simply the matrix elements in reverse order representing the coupling of the PWS test modes to the reflected traveling wave current. Thus, very few additional integrations are required to carry out the S-parameter analysis despite the introduction of an additional column and row to the matrix $[Z_{tot}^a]$ and an additional element to the vectors $[C_{tot}^a]$, $[T^a]$ and $[V_{inc}]$. If the same number of PWS expansion currents are used on the feed line in the two analyses, then only two additional matrix elements must be calculated in the S-parameter analysis as compared to the terminated line analysis. As will be seen subsequently most of the additional effort required for this analysis is in the form of matrix fill operations and a couple of additional algebraic operations.

Rewriting (36)-(38) to account for the extra unknown, T_c , and incorporating the aforementioned symmetry relation yields

$$[z^a][I^a] + ([z^c] + j[z^s])r_c + ([\bar{z}^c] + j[\bar{z}^s])T_c - [T^a]V^{ap} = -[z^c] + j[z^s] \quad (66)$$

$$-[c^a][I^a] - (c^c + jc^s)r_c - (c^c + jc^s)T_c + (y^a + y^b)V^{ap} + [c^b][I^b] = c^c - jc^s \quad (67)$$

$$[z^b][I^b] + [T^b]V^{ap} = 0 \quad (68)$$

where

$$\bar{z}_m^c = z_{(N_a+1)-m}^c \quad (69)$$

$$\bar{z}_m^s = z_{(N_a+1)-m}^s \quad (70)$$

$$m = 0, 1, 2, \dots, N_a, N_a + 1$$

All other quantities are defined as before in (39)-(52) with the appropriate change in matrix dimensions due to the change in the range of index m .

As before, it is worthwhile to consolidate some of the matrices above by defining

$$[z_{tot}^a] = [z_{mn}^a \mid (z_m^c + jz_m^s) \mid (\bar{z}_m^c + j\bar{z}_m^s)] \quad N_a + 2 \times N_a + 2 \quad \text{matrix} \quad (71)$$

$$[c_{tot}^a] = [c_n^a \mid (c_n^c + jc_n^s) \mid (c_n^c + jc_n^s)] \quad 1 \times N_a + 2 \quad \text{row vector} \quad (72)$$

$$[I_{tot}^a] = [I_n^a \mid r_c \mid T_c] \quad N_a + 2 \times 1 \quad \text{column vector} \quad (73)$$

$$m = 0, 1, 2, \dots, N_a, N_a + 1$$

$$n = 1, 2, \dots, N_a$$

With these definitions, (60)-(62) remain valid. It should be noted from (73) that Γ_c is the next to last element and T_c is the last element in $[I_{tot}^a]$.

Since the junction is symmetric, the S-parameters referenced to the center of the aperture are

$$S_{11} = S_{22} = -\Gamma_c \quad (74)$$

$$S_{21} = S_{12} = T_c \quad (75)$$

The input impedance can be easily calculated from the S-parameter analysis when the feed is terminated in an open circuit. Examining Figure 2.3c reveals that the relationship of the first $(N_a-1)/2$ PWS modes (assuming N_a is always odd) and the reflected traveling wave current is identical to that of the open ended feed analysis shown in Figure 2.3b. Thus, the matrix elements necessary to rigorously calculate the current reflection coefficient seen at the end of an open circuited microstrip line alone exist within $[Z_{tot}^a]$ and $[V_{inc}]$. The appropriate elements reside in the top $(N_a+1)/2$ rows of $[Z_{tot}^a]$ and $[V_{inc}]$ and columns one through $(N_a-1)/2$ and column N_a-1 of $[Z_{tot}^a]$. Letting

$$N = (N_a+1)/2 \quad (76)$$

$$[Z] = [z_{mn}^a \mid (z_m^a + jz_m^s)] \quad N \times N \quad (77)$$

$$[I] = [I_1, I_2, \dots, I_{N-1}, \Gamma_{oo}] \quad N \times 1 \quad (78)$$

$$[V] = [-z_m^c + jz_m^s] \quad N \times 1 \quad (79)$$

$$m = 0, 1, \dots, N-1$$

$$n = 1, 2, \dots, N-1$$

then Γ_{co} is the open circuit reflection coefficient for a microstrip line alone. Γ_{co} is found by solving

$$[Z][I] = [V] \quad (80)$$

With the S-parameters and Γ_{co} the input impedance, referenced to the aperture center, of an antenna terminated by an open circuited stub of length L_s can be easily found from

$$Z_{in} = Z_0 \frac{1 + \Gamma_{in}}{1 - \Gamma_{in}} \quad (81)$$

where

$$\Gamma_{in} = s_{11} + \frac{s_{12}s_{21}\Gamma_L}{1 - s_{22}\Gamma_L} \quad (82)$$

$$\Gamma_L = -\Gamma_{co} e^{-j2k_e^a L_s} \quad (83)$$

Dielectric Slab Green's Functions

From (39)-(50) it can be seen that the fields due to a given current in the presence of the grounded dielectric slab are required. The fields can be found by convolving the given basis current against

the appropriate Green's function. The required Green's functions are the \hat{y} - directed electric field and \hat{x} - directed magnetic field due to a \hat{y} - directed infinitesimal electric dipole at (x_o, y_o, d_b) and the same field components due to an \hat{x} - directed infinitesimal magnetic dipole at $(x_o, y_o, 0)$ for the grounded dielectric slab where the ground plane and dielectric to air interface is located at $z=0$ and $z=d_b$ respectively.

Figure 2.4 shows the nature, direction, and location of the two sources necessary to obtain the various Green's functions. The presence of the dielectric interface at $z=d_b$ gives rise to fields which cannot be decomposed into a single transverse electric (TE) or transverse magnetic (TM) mode. For the electric dipole of Figure 2.4a the fields are constructed from TM to \hat{y} ($A_y \hat{y}$) and TM to \hat{z} ($A_z \hat{z}$) vector potentials and analogously the fields due to the magnetic dipole of Figure 2.4b are formed from TE to \hat{x} ($F_x \hat{x}$) and TE to \hat{z} ($F_z \hat{z}$) vector potentials.

The vector potentials are derived using the Fourier transform method which is suitable for structures unbounded in one or more dimensions. By Fourier transforming the scalar wave equation for each of the above vector potential components with respect to x and y , the problem is reduced to a one dimensional Green's function problem in z . The x and y dependency of the fields are obtained by performing the inverse Fourier transform.

In the case of the \hat{y} - directed electric dipole of Figure 2.4a the scalar differential equations which must be solved are

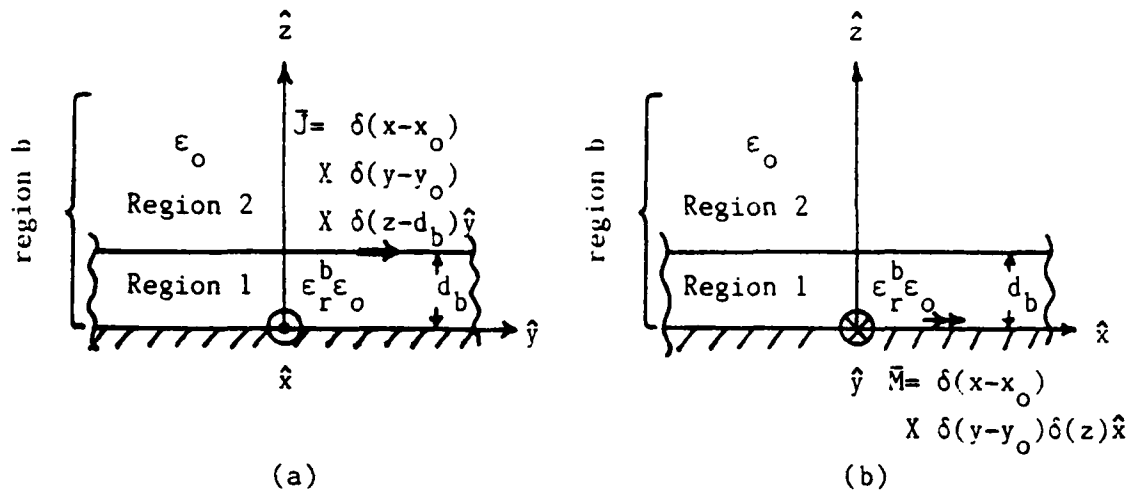


Figure 2.4 Orientation, location and type of current sources used to solve for the Green's functions in region b. (a) J-source (b) M-source

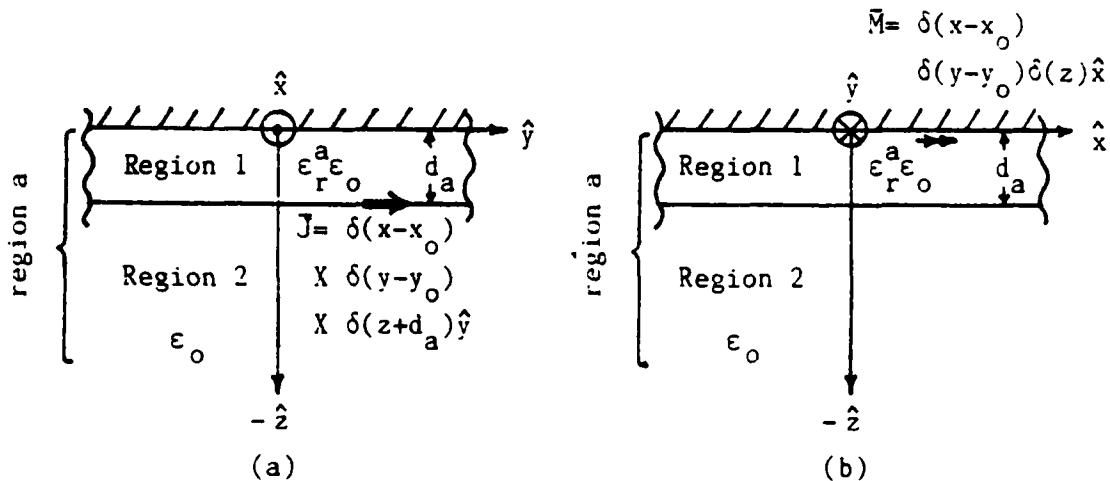


Figure 2.5 Orientation, location and type of current source used to solve for the Green's functions in region a. (a) J-source (b) M-source

$$[\nabla^2 + \epsilon_r^b k_o^2] A_{y1}(x, y, z) = -\delta(x-x_o) \delta(y-y_o) \delta(z-d_b), \quad 0 < z < d_b \quad (84a)$$

$$[\nabla^2 + \epsilon_r^b k_o^2] A_{z1}(x, y, z) = 0, \quad 0 < z < d_b \quad (84b)$$

$$[\nabla^2 + k_o^2] A_{y2}(x, y, z) = 0, \quad z > d_b \quad (84c)$$

$$[\nabla^2 + k_o^2] A_{z2}(x, y, z) = 0, \quad z > d_b \quad (84d)$$

where

$$k_o^2 = \omega^2 \epsilon_o \mu_o \quad (85)$$

The free space permittivity and permeability are ϵ_o and μ_o respectively.

The complex dielectric constant, which takes into account dielectric loss, is ϵ_r^b . Fourier transforming (84a)-(84d) with respect to x and y gives

$$[\frac{d^2}{dz^2} + k_{1b}^2] \tilde{A}_{y1}(k_x, k_y, z) = -\delta(z-d_b) e^{-j(k_x x_o + k_y y_o)}, \quad 0 < z < d_b \quad (86a)$$

$$[\frac{d^2}{dz^2} + k_{1b}^2] \tilde{A}_{z1}(k_x, k_y, z) = 0, \quad 0 < z < d_b \quad (86b)$$

$$[\frac{d^2}{dz^2} + k_2^2] \tilde{A}_{y2}(k_x, k_y, z) = 0, \quad z > d_b \quad (86c)$$

$$[\frac{d^2}{dz^2} + k_2^2] \tilde{A}_{z2}(k_x, k_y, z) = 0, \quad z > d_b \quad (86d)$$

where

$$\tilde{A}_{y1,2}(k_x, k_y, z) = \iint_{-\infty}^{\infty} A_{y1,2}(x, y, z) e^{-j(k_x x + k_y y)} dx dy \quad (87)$$

$$\tilde{A}_{z1,2}(k_x, k_y, z) = \iint_{-\infty}^{\infty} A_{z1,2}(x, y, z) e^{-j(k_x x + k_y y)} dx dy \quad (88)$$

$$k_{1b} = (\epsilon_r^b k_o^2 - \beta^2)^{1/2}, \quad \text{Im}\{k_{1b}\} < 0, \quad \text{Re}\{k_{1b}\} > 0 \quad (89)$$

$$k_2 = (k_o^2 - \beta^2)^{1/2}, \quad \text{Im}\{k_2\} < 0, \quad \text{Re}\{k_2\} > 0 \quad (90)$$

$$\beta^2 = k_x^2 + k_y^2 \quad (91)$$

The quantities k_x and k_y are the two independent separation constants in the separation equations given in (89) and (90). The sign on the imaginary part of k_{1b} and k_2 is chosen to guarantee convergence of the integrals in (87) and (88) and the sign on the real part is necessary to remain on the same branch as determined by the sign on the imaginary part [5]. Solving (86a)-(86d) subject to the boundary conditions yields the magnetic vector potential components in the spectral domain.

$$\tilde{A}_{y1}(k_x, k_y, z) = \frac{1}{T_e^b} \sin(k_{1b}z) e^{-j(k_x x_o + k_y y_o)} \quad (92)$$

$$\tilde{A}_{z1}(k_x, k_y, z) = \frac{k_y(\epsilon_r^b - 1) \sin(k_{1b}d_b)}{T_e^b T_m^b} \cos(k_{1b}z) e^{-j(k_x x_o + k_y y_o)} \quad (93)$$

$$\tilde{A}_{y2}(k_x, k_y, z) = \frac{\sin(k_{1b}d_b)}{T_e^b} e^{-jk_2(z-d_b)} e^{-j(k_x x_o + k_y y_o)} \quad (94)$$

$$\tilde{A}_{z2}(k_x, k_y, z) = \frac{k_y(\epsilon_r^b - 1) \sin(k_{1b}d_b) \cos(k_{1b}d_b)}{T_e^b T_m^b} e^{-jk_2(z-d_b)} \times e^{-j(k_x x_o + k_y y_o)} \quad (95)$$

$$T_e^b = k_{1b} \cos(k_{1b}d_b) + jk_2 \sin(k_{1b}d_b) \quad (96)$$

$$T_m^b = \epsilon_r^b k_2 \cos(k_{1b}d_b) + jk_{1b} \sin(k_{1b}d_b) \quad (97)$$

The transformed electric and magnetic field quantities of interest are easily obtained from

$$\tilde{E}_y^b(k_x, k_y, z) = \frac{1}{j\omega \epsilon_r \epsilon_0} [(\epsilon_r^b k_o^2 - k_y^2) \tilde{A}_y + jk_y \frac{d}{dz} \tilde{A}_z] \quad (98)$$

$$\tilde{H}_x^b(k_x, k_y, z) = -\frac{d}{dz} \tilde{A}_y + jk_y \tilde{A}_z \quad (99)$$

Thus, the required Green's functions in the space domain due to the \hat{y} - directed infinitesimal dipole are: (1) the \hat{y} - directed electric field at $z=d_b$

$$G_{EJyy}^b(x, y, d_b | x_o, y_o, d_b) = \iint_{-\infty}^{\infty} Q_{EJyy}^b(k_x, k_y) e^{j(k_x(x-x_o) + k_y(y-y_o))} dk_x dk_y \quad (100)$$

$$Q_{EJyy}^b(k_x, k_y) = -j \frac{z_o}{4\pi^2 k_o} \frac{(\epsilon_r^b k_o^2 - k_y^2) k_2 \cos(k_1 b d_b) + j(k_o^2 - k_y^2) k_1 b \sin(k_1 b d_b)}{T_e^b T_m^b} \quad (101)$$

$$x \sin(k_1 b d_b)$$

where $z_o = (\mu_o / \epsilon_o)^{1/2}$ and (2) the \hat{x} - directed magnetic field at $z=0$

$$G_{HJxy}^b(x, y, 0 | x_o, y_o, d_b) = \iint_{-\infty}^{\infty} Q_{HJxy}^b(k_x, k_y) e^{j(k_x(x-x_o) + k_y(y-y_o))} dk_x dk_y \quad (102)$$

$$Q_{HJxy}^b(k_x, k_y) = \frac{1}{4\pi^2} \frac{-\epsilon_r^b k_1 b k_2 \cos(k_1 b d_b) + j(k_y^2 (\epsilon_r^b - 1) - k_1 b^2) \sin(k_1 b d_b)}{T_e^b T_m^b} \quad (103)$$

The above Green's functions are appropriate for finding fields in region b due to the currents on the antenna element. The Green's functions necessary to find the fields in region a due to the feed line currents are determined from the configuration of Figure 2.5a. The fields in this case are easily determined from (100)-(103) by a simple coordinate transformation and replacing d_b with d_a and ϵ_r^b with ϵ_r^a . Thus, the \hat{y} - directed electric field at $z=-d_a$ is

$$G_{EJyy}^a(x, y, -d_a | x_o, y_o, -d_a) = \iint_{-\infty}^{\infty} Q_{EJyy}^b(k_x, k_y) e^{j(k_x(x-x_o) + k_y(y-y_o))} dk_x dk_y \quad (104)$$

$$Q_{EJyy}^a(k_x, k_y) = Q_{EJyy}^b(k_x, k_y) |_{\epsilon_r^b + \epsilon_r^a, d_b + d_a} \quad (\text{see eqn. 101}) \quad (105)$$

and the \hat{x} - directed magnetic field at $z=0$ is

$$G_{HJxy}^a(x, y, 0 | x_o, y_o, -d_a) = \iint_{-\infty}^{\infty} Q_{HJxy}^a(k_x, k_y) e^{j(k_x(x-x_o) + k_y(y-y_o))} dk_x dk_y \quad (106)$$

$$Q_{HJxy}^a(k_x, k_y) = -Q_{HJxy}^b(k_x, k_y) |_{\epsilon_r^b + \epsilon_r^a, d_b + d_a} \quad (\text{see eqn. 103}) \quad (107)$$

In the case of the \hat{x} - directed magnetic dipole at $z=0$ in Figure 2.4b the same procedure as above is followed to solve for the electric vector potential. The Fourier transformed differential equations for the electric vector potential components are

$$[\frac{d^2}{dz^2} + k_{1b}^2] \bar{F}_{x1}(k_x, k_y, z) = -\delta(z) e^{-j(k_x x_o + k_y y_o)}, \quad 0 < z < d_b \quad (108a)$$

$$\left[\frac{d^2}{dz^2} + k_{1b}^2 \right] \tilde{F}_{z1}(k_x, k_y, z) = 0, \quad 0 < z < d_b \quad (108b)$$

$$\left[\frac{d^2}{dz^2} + k_2^2 \right] \tilde{F}_{x2}(k_x, k_y, z) = 0, \quad z > d_b \quad (108c)$$

$$\left[\frac{d^2}{dz^2} + k_2^2 \right] \tilde{F}_{z2}(k_x, k_y, z) = 0, \quad z > d_b \quad (108d)$$

where

$$\tilde{F}_{x1,2}(k_x, k_y, z) \longleftrightarrow F_{x1,2}(x, y, z) \quad (109)$$

$$\tilde{F}_{z1,2}(k_x, k_y, z) \longleftrightarrow F_{z1,2}(x, y, z) \quad (110)$$

Solving (108a)-(108d) and applying the boundary conditions gives the electric vector potential components in the spectral domain given below.

$$\tilde{F}_{x1}(k_x, k_y, z) = \left[\frac{\epsilon_r^b k_2 \sin(k_{1b} d_b) - j k_{1b} \cos(k_{1b} d_b)}{k_{1b} T_m^b} \right] \cos(k_{1b} z) \quad (111)$$

$$- \frac{\sin(k_{1b} z)}{k_{1b}} e^{-j(k_x x_o + k_y y_o)}$$

$$\tilde{F}_{z1}(k_x, k_y, z) = \frac{k_x (\epsilon_r^b - 1)}{T_e^b T_m^b} \sin(k_{1b} z) e^{-j(k_x x_o + k_y y_o)} \quad (112)$$

$$\tilde{F}_{x2}(k_x, k_y, z) = -j \frac{\epsilon_r^b}{T_m^b} e^{-j k_2 (z - d_b)} e^{-j(k_x x_o + k_y y_o)} \quad (113)$$

$$\tilde{F}_{z2}(k_x, k_y, z) = \frac{k_x (\epsilon_r^b - 1) \sin(k_{1b} d_b)}{T_e^b T_m^b} e^{-j k_2 (z - d_b)} e^{-j(k_x x_o + k_y y_o)} \quad (114)$$

The two field quantities desired are obtained from

$$\tilde{E}_y^b(k_x, k_y, z) = -\frac{d}{dz}\tilde{F}_x + jk_x\tilde{F}_z \quad (115)$$

$$\tilde{H}_x^b(k_x, k_y, z) = \frac{1}{j\omega\mu_0} [(\epsilon_r^b k_o^2 - k_x^2)\tilde{F}_x + jk_x \frac{d}{dz}\tilde{F}_z] \quad (116)$$

From (111), (112), (115) and (116) the necessary Green's functions in the space domain due to the \hat{x} - directed infinitesimal magnetic dipole can be readily found. These are: (1) the \hat{x} - directed magnetic field at $z = 0$

$$G_{HMxx}^b(x, y, 0 | x_o, y_o, 0) = \iint_{-\infty}^{\infty} Q_{HMxx}^b(k_x, k_y) e^{j(k_x(x-x_o) + k_y(y-y_o))} dk_x dk_y \quad (117)$$

$$Q_{HMxx}^b(k_x, k_y) = \frac{-j}{4\pi^2 k_o^2 Z_o} \frac{1}{k_{1b} T_b^b e^{T_m^b}} [jk_x^2 k_{1b}^2 (\epsilon_r^b - 1) + (\epsilon_r^b k_o^2 - k_x^2) \times \{k_{1b} k_2 (\epsilon_r^b + 1) \sin(k_{1b} d_b) \cos(k_{1b} d_b) + j(\epsilon_r^b k_2^2 \sin^2(k_{1b} d_b) - k_{1b}^2 \cos^2(k_{1b} d_b))\}] \quad (118)$$

(2) the \hat{y} - directed electric field at $z = d_b$

$$G_{EMyx}^b(x, y, d_b | x_o, y_o, 0) = \iint_{-\infty}^{\infty} Q_{EMyx}^b(k_x, k_y) e^{j(k_x(x-x_o) + k_y(y-y_o))} dk_x dk_y \quad (119)$$

$$Q_{EMyx}^b(k_x, k_y) = -Q_{HJxy}^b(k_x, k_y) \quad (\text{see eqn. 103}) \quad (120)$$

Equation (120) follows from reciprocity.

As before, the Green's functions appropriate for region a shown in Figure 2.5b can be formed from those given in (117)-(120). These Green's functions are the \hat{x} - directed magnetic field at $z = 0$

$$G_{HMxx}^a(x, y, 0 | x_o, y_o, 0) = \iint_{-\infty}^{\infty} Q_{HMxx}^a(k_x, k_y) e^{j(k_x(x-x_o) + k_y(y-y_o))} dk_x dk_y \quad (121)$$

$$Q_{HMxx}^a(k_x, k_y) = Q_{HMxx}^b(k_x, k_y) \Big|_{\epsilon_r^b \rightarrow \epsilon_r^a, d_b \rightarrow d_a} \quad (\text{see eqn. 118}) \quad (122)$$

and the \hat{y} - directed electric field at $z = -d_a$

$$G_{EMyx}^a(x, y, -d_a | x_o, y_o, 0) = \iint_{-\infty}^{\infty} Q_{EMyx}^a(k_x, k_y) e^{j(k_x(x-x_o) + k_y(y-y_o))} dk_x dk_y \quad (123)$$

$$Q_{EMyx}^a(k_x, k_y) = -Q_{EMyx}^b(k_x, k_y) \Big|_{\epsilon_r^b \rightarrow \epsilon_r^a, d_b \rightarrow d_a} \quad (\text{see eqn. 120}) \quad (124)$$

Matrix Element Expressions

With these Green's Functions the matrix elements in (39)-(50) can be fully defined. In (39) $E_a^y(J_n^a)$ is the \hat{y} - component of the electric field at $z = -d_a$ due to the basis current J_n^a in the presence of the dielectric slab. This field is obtained by convolving the Green's function given in (104) against J_n^a as shown below.

(125)

$$E_a^y(J_n^a) = \int_{y_o} \int_{x_o} J_n^a(x_o, y_o) \iint_{-\infty}^{\infty} Q_{EMyx}^a(k_x, k_y) e^{j(k_x(x-x_o) + k_y(y-y_o))} dk_x dk_y dx_o dy_o$$

Substituting (125) into (39) yields

$$z_{mn}^a = - \iint_{y \times x} \hat{J}_m^a(x, y) \iint_{y_o \times o} J_n^a(x_o, y_o) \iint_{-\infty}^{\infty} Q_E^a e^{j(k_x(x-x_o) + k_y(y-y_o))} dk_x dk_y dx_o dy_o dx dy \quad (126)$$

or

$$z_{mn}^a = - \iint_{-\infty}^{\infty} Q_E^a e^{j(k_x(x-x_o) + k_y(y-y_o))} \hat{J}_m^a(k_x, k_y) \hat{J}_n^a(k_x, k_y) dk_x dk_y \quad (127)$$

where

$$\hat{J}_n^a(k_x, k_y) = \iint_{y_o \times x_o} J_n^a(x, y) e^{-j(k_x(x-x_o) + k_y(y-y_o))} dx_o dy_o \quad (128a)$$

$$\hat{J}_m^a(k_x, k_y) = \iint_{y \times x} \hat{J}_m^a(x, y) e^{j(k_x(x-x_o) + k_y(y-y_o))} dx dy \quad (128b)$$

Thus, the six fold integration in (126) can be reduced to a double integral by Fourier transforming the basis and test currents analytically as defined in (128). Note that (128b) is only valid for real currents. The integration in (127) must be carried out numerically so it is advantageous to convert the double infinite integral in the k_x, k_y plane to a single infinite integral and a finite integral by converting to polar coordinates [6]. Letting

$$k_x = \beta \cos \alpha$$

$$k_y = \beta \sin \alpha$$

(127) becomes

$$z_{mn}^a = - \int_0^{2\pi} \int_0^{\infty} Q_E^a e^{j(k_x(x-x_o) + k_y(y-y_o))} \hat{J}_m^a(k_x, k_y) \hat{J}_n^a(k_x, k_y) \beta d\beta d\alpha \quad (129)$$

A further simplification can be realized by noting that the Q functions are even in k_x and k_y allowing one to integrate on α from 0 to $\pi/2$ only [6] as shown below.

$$z_{mn}^a = -4 \int_0^{\pi/2} \int_0^{\infty} Q_E^a J_{yy}(k_x, k_y) \operatorname{Re} \{ \hat{J}_m^a(k_x) \hat{J}_n^a(k_x) \} \operatorname{Re} \{ \hat{J}_m^a(k_y) \hat{J}_n^a(k_y) \} \beta d\beta d\alpha \quad (130)$$

where

$$\hat{J}_n^a(k_x, k_y) = \hat{J}_n^a(k_x) \hat{J}_n^a(k_y) \quad (131)$$

Defining Fourier transform pairs of the other currents as

$$J_c^a(x, y) \longleftrightarrow \hat{J}_c^a(k_x) \hat{J}_c^a(k_y) \quad (132)$$

$$J_s^a(x, y) \longleftrightarrow \hat{J}_s^a(k_x) \hat{J}_s^a(k_y) \quad (133)$$

$$M^{ap}(x, y) \longleftrightarrow \hat{M}^{ap}(k_x) \hat{M}^{ap}(k_y) \quad (134)$$

$$J_1^b(x, y) \longleftrightarrow \hat{J}_1^b(k_x) \hat{J}_1^b(k_y) \quad (135)$$

the remaining matrix elements can be written as

$$z_m^c = -4 \int_0^{\pi/2} \int_0^{\infty} Q_E^a J_{yy}(k_x, k_y) \operatorname{Re} \{ \hat{J}_m^a(k_x) \hat{J}_c^a(k_x) \} \operatorname{Re} \{ \hat{J}_m^a(k_y) \hat{J}_c^a(k_y) \} \beta d\beta d\alpha \quad (137)$$

$$z_m^s = -4 \int_0^{\pi/2} \int_0^{\infty} Q_E^a J_{yy}(k_x, k_y) \operatorname{Re} \{ \hat{J}_m^a(k_x) \hat{J}_s^a(k_x) \} \operatorname{Re} \{ \hat{J}_m^a(k_y) \hat{J}_s^a(k_y) \} \beta d\beta d\alpha \quad (138)$$

$$z_{k1}^b = -4 \int_0^{\pi/2} \int_0^{\infty} Q_E^b J_{yy}(k_x, k_y) \operatorname{Re} \{ \hat{J}_k^b(k_x) \hat{J}_1^b(k_x) \} \operatorname{Re} \{ \hat{J}_k^b(k_y) \hat{J}_1^b(k_y) \} \beta d\beta d\alpha \quad (139)$$

$$y^a = -4 \int_0^{\pi/2} \int_0^{\infty} Q_H^a M_{xx}(k_x, k_y) |\hat{M}^{ap}(k_x)|^2 |\hat{M}^{ap}(k_y)|^2 \beta d\beta d\alpha \quad (140)$$

$$y^b = -4 \int_0^{\pi/2} \int_0^{\infty} Q_{HMxx}^b(k_x, k_y) |\tilde{M}^{ap}(k_x)|^2 |\tilde{M}^{ap}(k_y)|^2 \beta d\beta da \quad (141)$$

$$c_n^a = 4 \int_0^{\pi/2} \int_0^{\infty} Q_{HJxy}^a(k_x, k_y) \operatorname{Re}\{\tilde{M}^{ap}(k_x) \tilde{J}_n^a(k_x)\} \operatorname{Re}\{\tilde{M}^{ap}(k_y) \tilde{J}_n^a(k_y)\} \beta d\beta da \quad (142)$$

$$c_c^c = 4 \int_0^{\pi/2} \int_0^{\infty} Q_{HJxy}^a(k_x, k_y) \operatorname{Re}\{\tilde{M}^{ap}(k_x) \tilde{J}_c^a(k_x)\} \operatorname{Re}\{\tilde{M}^{ap}(k_y) \tilde{J}_c^a(k_y)\} \beta d\beta da \quad (143)$$

$$c_s^s = 4 \int_0^{\pi/2} \int_0^{\infty} Q_{HJxy}^a(k_x, k_y) \operatorname{Re}\{\tilde{M}^{ap}(k_x) \tilde{J}_s^a(k_x)\} \operatorname{Re}\{\tilde{M}^{ap}(k_y) \tilde{J}_s^a(k_y)\} \beta d\beta da \quad (144)$$

$$c_1^b = 4 \int_0^{\pi/2} \int_0^{\infty} Q_{HJxy}^b(k_x, k_y) \operatorname{Re}\{\tilde{M}^{ap}(k_x) \tilde{J}_1^b(k_x)\} \operatorname{Re}\{\tilde{M}^{ap}(k_y) \tilde{J}_1^b(k_y)\} \beta d\beta da \quad (145)$$

$$m = 0, 1, 2, \dots, N_a \quad n = 1, 2, \dots, N_a$$

$$k = 1, 2, \dots, N_b \quad l = 1, 2, \dots, N_b$$

The elements t_k^b and t_m^a are related to c_1^b and c_n^a by (58) and (59) respectively.

Numerical Considerations

The integrals in (130) and (137)-(145) must be evaluated numerically. The numerical integration routine used was a modification of a routine written by D. M. Pozar to analyze a rectangular microstrip antenna fed by an ideal impulse current source [6]. This routine employs a 10 point Gaussian quadrature integration scheme. A special consideration common to all of the integrations is the presence of simple poles determined by the zeroes of (96) and (97) which are a function of β only. (In region a the poles are determined from (96) and

(97) where d_b is replaced by d_a and ϵ_r^b by ϵ_r^a .) These poles correspond to the TE and TM surface wave modes respectively. The poles are first located by the Newton-Raphson method, where the real part of the pole always lies between k_o and $(\epsilon_r)^{1/2} k_o$. The integration on β is then carried out by numerically integrating on β up to within $\Delta = .001 k_o$ of the real part of the pole (β_o). The integration from $\beta_o - \Delta$ to $\beta_o + \Delta$ is performed analytically. The details of this integration are given in [6]. This cycle is continued until the last pole is encountered. The remaining portion of the integration is calculated numerically until convergence is achieved. Convergence is attained when at least half the elements in a given vector change by less than .5% over an integration interval of $50 k_o$. This usually occurs somewhere in the interval $100 k_o \leq \beta \leq 200 k_o$.

By the symmetry properties of Green's functions and Toeplitz symmetries, which occur due to the infinite extent of the grounded dielectric slab, only a single row or column of any matrix must be calculated. The above integration routine was modified to calculate an entire row or column with a single call of the integration routine. This greatly improves the computation time of the analysis because an entire vector of about 10 elements or less can be calculated almost as fast as a single element. This is due to the fact that all the integrands can be factored into two terms. One term, $T_{cnst}(k_x, k_y)$, is common to all the elements in the vector and represents a vast majority of the integrand. The other term, $T_{var}(k_x, k_y, m, n)$, differs from element

to element but is generally simple in form and in most cases is a single cosine term of the form, $\cos k_y(y_n - y_m)$ (where y_n and y_m are the y positions of the basis and test modes). Therefore, most of the integrand can be evaluated just once at each point, (k_{x0}, k_{y0}) , and the value of the total integrand for each element in the vector at (k_{x0}, k_{y0}) is then given by

$$I_T(k_{x0}, k_{y0}, m, n) = T_{\text{cnst}}(k_{x0}, k_{y0}) T_{\text{var}}(k_{x0}, k_{y0}, m, n) \quad (146)$$

To evaluate $T_{\text{var}}(k_{x0}, k_{y0}, m, n)$ N times ($N \leq 10$) takes far less time than to evaluate $T_{\text{cnst}}(k_{x0}, k_{y0})$ just once so the entire vector can be calculated nearly as fast as a single element.

Due to the complexity of the analysis various tests were performed to assess the validity of the numerical results. These tests included comparisons between numerical and analytic results for various limiting cases for which analytic solutions were possible and comparisons of numerical results with numerical results provided by D. M. Pozar and R. W. Jackson from programs which have been proven to be reliable. The latter type of comparisons confirmed the accuracy of the z_{mn}^a , z_{kl}^b , z_m^c , z_m^s elements. The y^a and y^b terms were validated by comparing the results to analytic solutions for the self impedance of a narrow slot with a PWS E-field aperture distribution in a ground plane in free space and in a very thick grounded dielectric slab. In the latter case the analytic solution is obtained by assuming the slot is in a homogeneous

medium with an effective dielectric constant, $\epsilon_{re} = (\epsilon_r + 1)/2$. In both of these cases the analytic and numerical results were in close agreement. The c_n^a element was checked by calculating in closed form the coupling between a short, narrow slot in a ground plane with a cosine aperture distribution and a short PWS dipole in the far field of the slot. Again the two solutions compared favorably.

Lastly, studies were conducted to determine the number and length of the current expansion modes necessary to obtain stable solutions. From these studies it was determined that five PWS modes on the patch, a traveling wave mode length of five feed line wavelengths, i.e., $5\lambda_f$, and a density of approximately seven PWS modes per $\lambda_f/2$ starting $\lambda_f/4$ prior to the aperture center were adequate for convergence in the range of the material parameters studied. In the case of the terminated line analysis the PWS mode density was held approximately constant for all stub lengths and in the case of the S-parameter analysis seven PWS expansion modes are used on the feedline from $y = -\lambda_f/4$ to $y = \lambda_f/4$.

CHAPTER III

RESULTS

In all subsequent input impedance plots certain conventions are followed. A measured impedance locus is denoted by a solid curve and the frequency, given in megahertz, is marked on the locus in 25 MHz intervals. Calculated input impedance points are given in 25 MHz steps and are connected by a best fit dashed circle. Both the measured and calculated input impedances are phase referenced to the center of the aperture. Empirical phase referencing was achieved by constructing a reference microstrip line of the appropriate length and shorting the end to the ground plane with a wide strip of copper foil.

Figure 3.1 shows a measured input impedance plot and various calculated points. The antenna and feed dielectric substrates were both Oak 601 with a nominal dielectric constant of 2.54 and a measured thickness of .16 cm. The antenna dimensions were 4.0 cm (resonant dimension) by 3.0 cm. The slot was 1.12 cm long by .155 cm wide. The microstrip feed line was .442 cm wide and extended 2.0 cm beyond the center of the aperture. Three sets of calculated data points are shown. The points defined by open squares were obtained assuming a cosine aperture E-field distribution ($k_{ap} = \pi/L_{ap}$ in eqn. 12) whereas the open and filled circles result from a PWS aperture E-field distribution. The input impedance data indicated by open circles was calculated using the

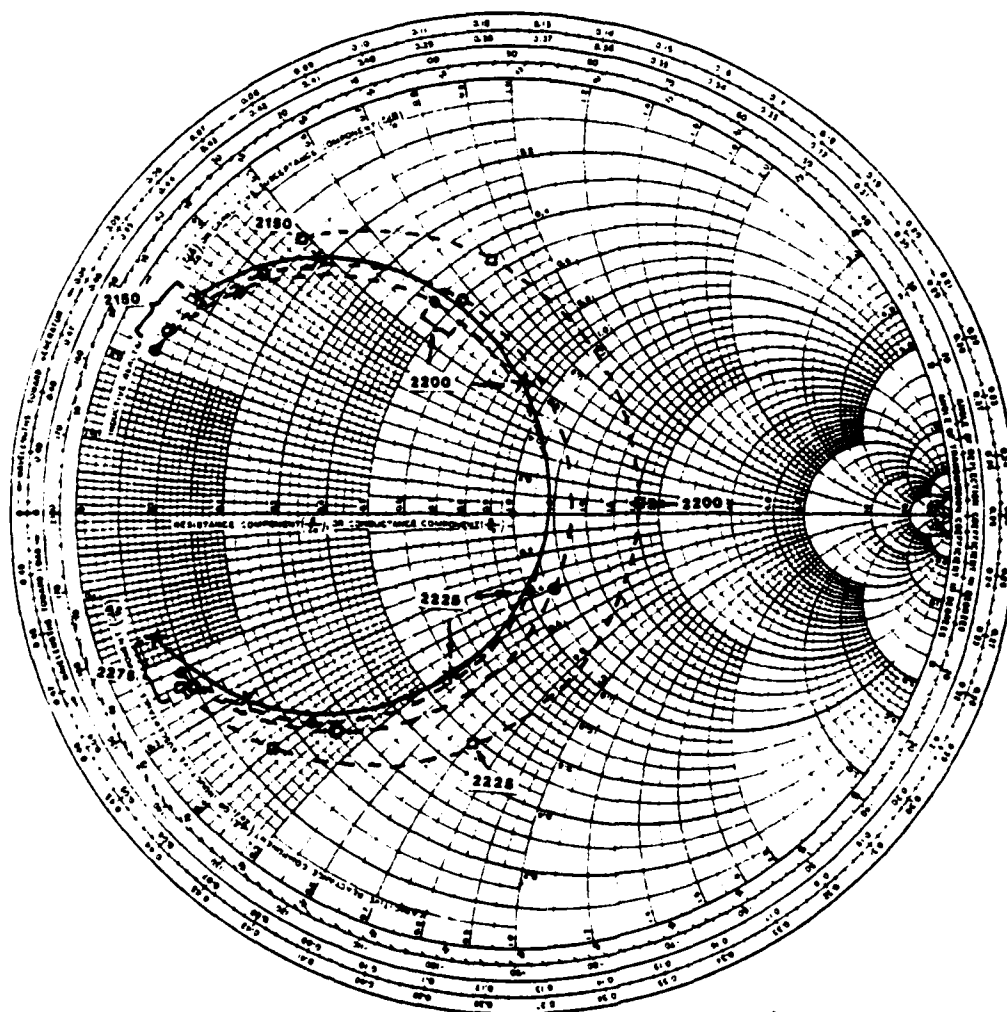


Figure 3.1 Measured versus calculated input impedance of an aperture coupled microstrip antenna with low dielectric constant feed substrate. \square = cosine E-field aperture distribution, direct method of calculation, \circ = PWS E-field aperture distribution, direct method of calculation, \bullet = PWS E-field aperture distribution, S-parameter method of calculation. ($\epsilon_r^b = 2.54$, $d_b = .16\text{cm}$, $L_p = 4.0\text{cm}$, $W_p = 3.0\text{cm}$,

$x_{os} = 0.0\text{cm}$, $y_{os} = 0.0\text{cm}$, $L_{ap} = 1.12\text{cm}$, $W_{ap} = .155\text{cm}$, $\epsilon_r^a = 2.54$, $d_a = .16\text{cm}$, $W_f = .442\text{cm}$, $L_s = 2.0\text{cm}$)

first scheme discussed in Chapter II where the feed line is terminated in an open circuit (to be called the direct method). The filled circles were calculated by the S-parameter method discussed in the second section of chapter two. In the case of the PWS aperture distribution the parameter k_{ap} in eqn. 12 was chosen to be the arithmetic average of the effective wave numbers for the feed and antenna regions, i.e., $k_{ap} = (k_e^a + k_e^b)/2$. This results in an aperture E-field distribution which is roughly triangular for the electrically short apertures used in these antennas.

The PWS aperture distribution yields significantly closer agreement with measured values than the cosine distribution. The results obtained with the direct method and the S-parameter method are approximately equivalent but the latter appears to match the measured results slightly better. Although the comparison between analytic and experimental results is good, even better agreement could be obtained by varying the dielectric constant within the manufacturer's specifications and adjusting slightly the reference plane which is empirically only approximately known.

To further confirm the validity of the PWS aperture distribution the same comparison as above is shown in Figure 3.2 for an antenna with a high dielectric constant feed substrate. The antenna substrate and dimensions are the same as above but Duroid 6010.2 ($\epsilon_r = 10.2$, $d_a = .1325\text{cm}$) was used for the feed substrate. The aperture dimensions in this case were $.913 \times .108\text{ cm}$ and the feed width and stub length beyond the

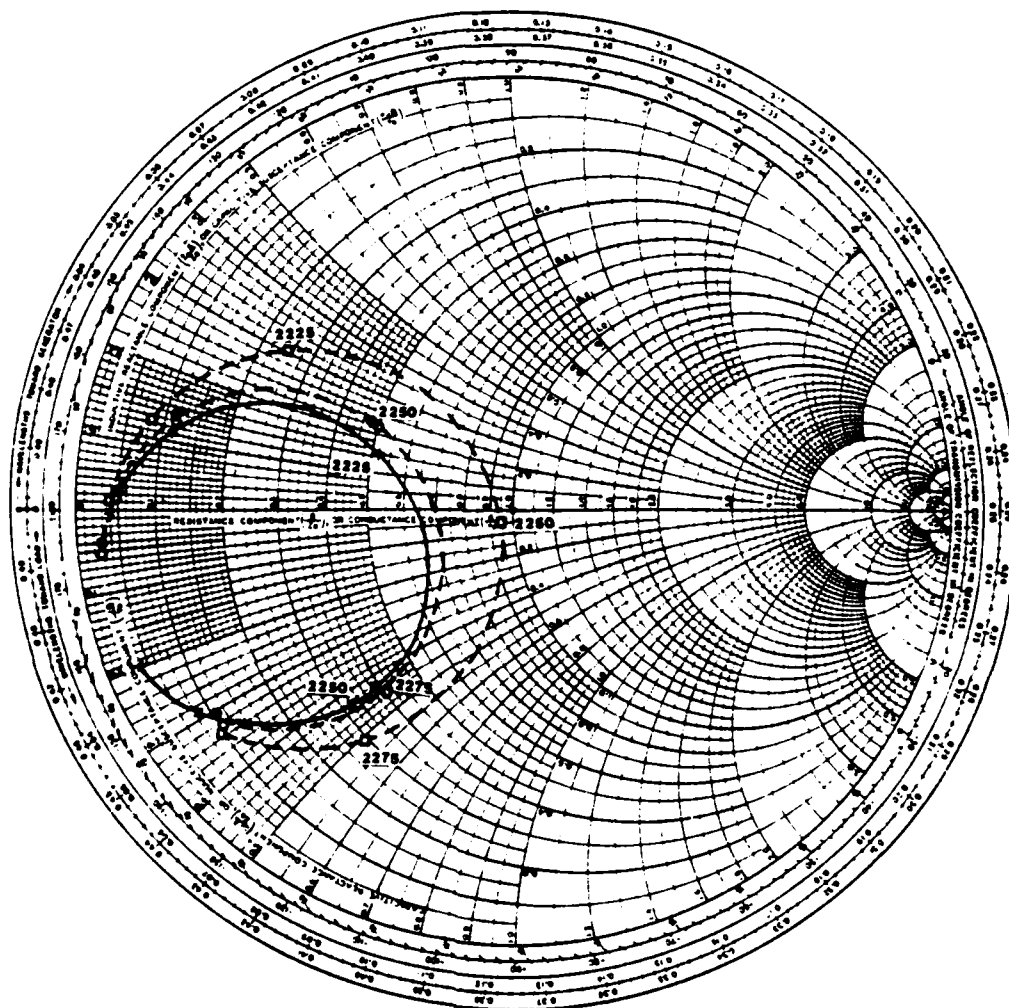


Figure 3.2 Measured versus calculated input impedance of an aperture coupled microstrip antenna with high dielectric constant feed substrate. □ = cosine E-field aperture distribution, direct method of calculation, ○ = PWS E-field aperture distribution, direct method of calculation, ● = PWS E-field aperture distribution, S-parameter method of calculation.

$$\begin{aligned}
 & (\epsilon_r^b = 2.54, d_b = 0.16\text{cm}, L_p = 4.0\text{cm}, W_p = 3.0\text{cm}, x_{os} = 0.0\text{cm}, y_{os} = 0.0\text{cm}, \\
 & L_{ap} = 0.913\text{cm}, W_{ap} = 0.108\text{cm}, \epsilon_r^a = 10.2, d_a = 0.1325\text{cm}, W_f = 0.116\text{cm}, L_s = 1.107\text{cm})
 \end{aligned}$$

Table 3.1 Calculated S-parameters for the antenna of figure 3.1.

Frequency (MHz)	S_{11}	S_{21}	$1-S_{11}$
2150	.06+j.18	.94-j.20	.94-j.18
2175	.11+j.22	.89-j.23	.89-j.22
2200	.25+j.23	.74-j.24	.75-j.23
2225	.34-j.05	.66+j.04	.66+j.05
2250	.12-j.11	.88+j.10	.88+j.11
2275	.04-j.05	.96+j.04	.96+j.05

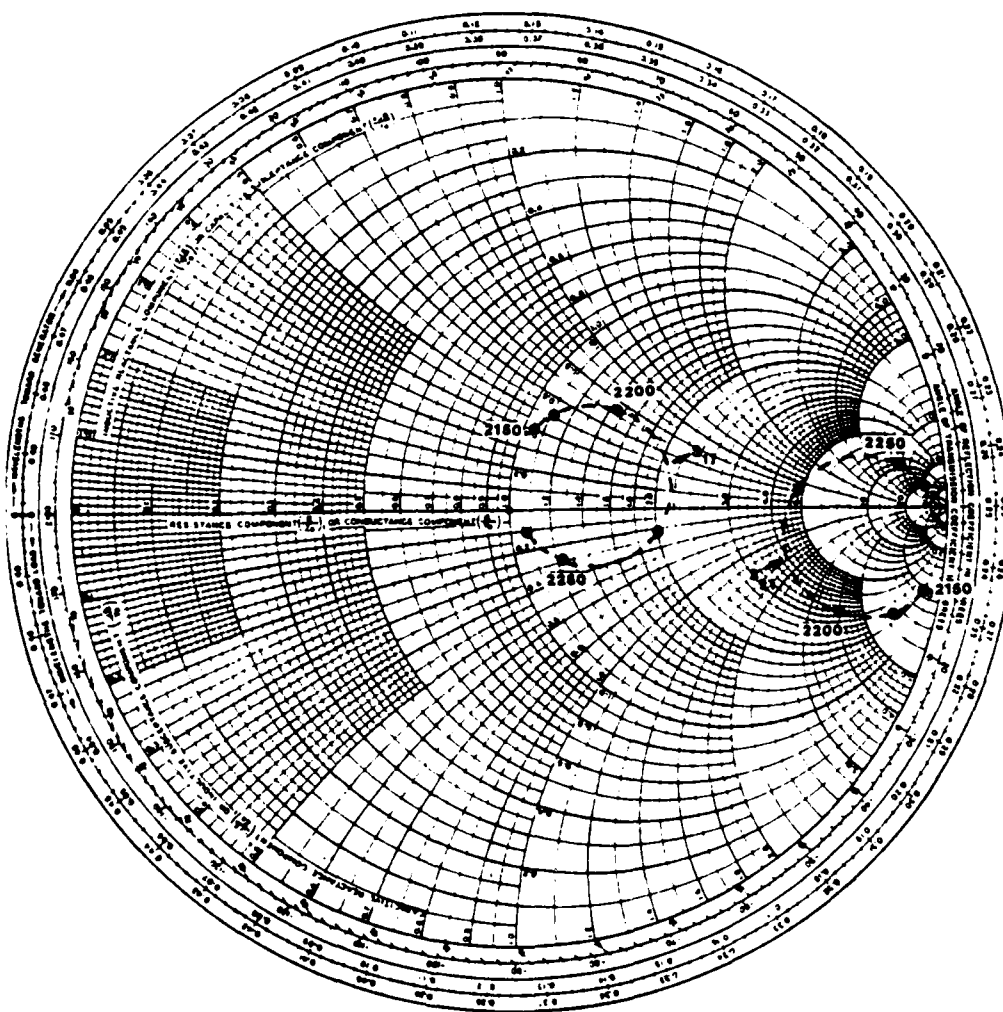


Figure 3.3 Calculated S-parameter plot for the antenna of figure 3.1.

Table 3.2 Calculated S-parameters for the antenna of figure 3.2.

Frequency (MHz)	S_{11}	S_{21}	$1-S_{11}$
2175	.03+j.19	.96-j.12	.97-j.19
2200	.05+j.21	.94-j.13	.95-j.21
2225	.10+j.24	.90-j.16	.90-j.24
2250	.23+j.20	.76-j.12	.77-j.20
2275	.15-j.01	.85+j.08	.85+j.01
2300	.04+j.04	.95+j.04	.96-j.04
2325	.02+j.07	.98+j.01	.98-j.07

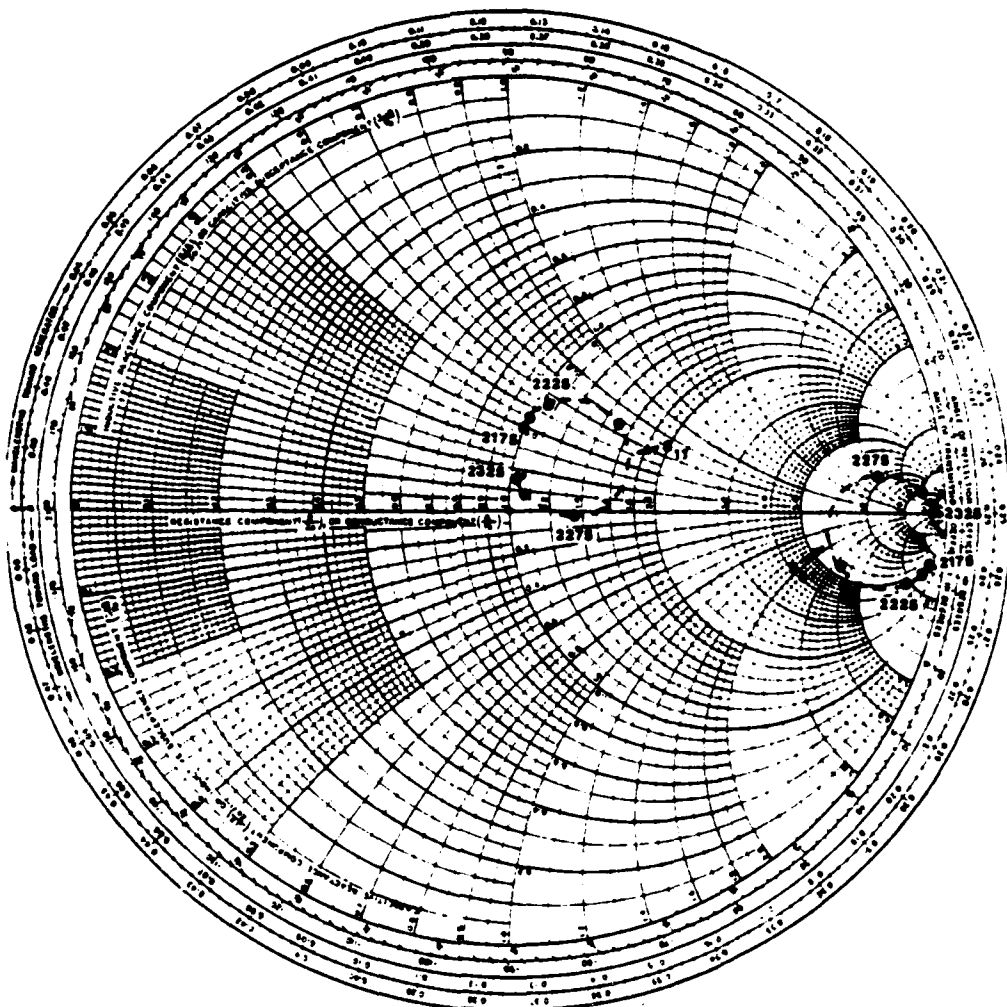


Figure 3.4 Calculated S-parameter plot for the antenna of figure 3.2.

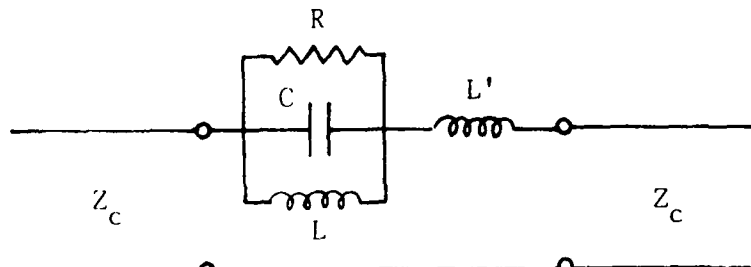


Figure 3.5 Equivalent two-port network for an aperture backed by a patch antenna in the ground plane of a microstripline.

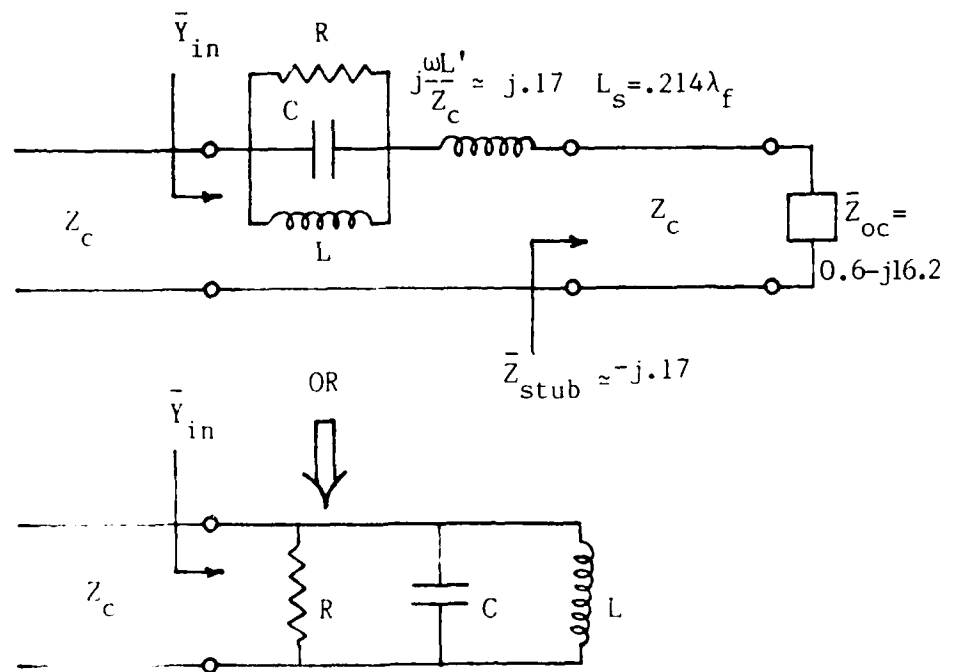


Figure 3.6 Equivalent circuit for the antenna of figure 3.1.

plotted on an admittance chart. This is to be expected based on the proposed model. Figure 3.6 shows a circuit model for the antenna of Figure 3.1. From the S-parameter analysis the reflection coefficient at the end of open ended microstrip line with the dimensions given in Figure 3.1 at 2.2 GHz equals $.99-j.12$ or equivalently \bar{Z}_{oc} (bar indicates normalized impedance) equals $0.6-j16.2$. The stub length beyond the center of the aperture at 2.2 GHz equals $.214\lambda_f$, where λ_f is the feed line wavelength ($\lambda_f=2\pi/k_e^a$). Therefore, the normalized impedance looking into the stub at the center of the aperture, \bar{Z}_{stub} , is $.002-j.17$ or $\bar{Z}_{stub} \approx -j.17$. Presumably, the capacitive reactance cancels the series inductive reactance over the bandwidth of the parallel RLC network yielding the bottom circuit of Figure 3.6. The input admittance of this circuit follows a constant conductance circle.

Three parameter studies were carried out both empirically and analytically with the antenna of Figure 3.1. These parameters were selected due to the reasonable ease and accuracy with which they could be varied experimentally.

The effect of stub length, i.e., the length of feed line beyond the center of the aperture, on the input impedance locus was examined. The measured loci versus stub length are shown in Figure 3.7. As the length of the open circuited stub is decreased, from an initial dimension of $.214\lambda_f$, the input impedance at any given frequency moves counterclockwise along a constant resistance circle towards the open circuit point on the Smith Chart. Since the aperture looks like a

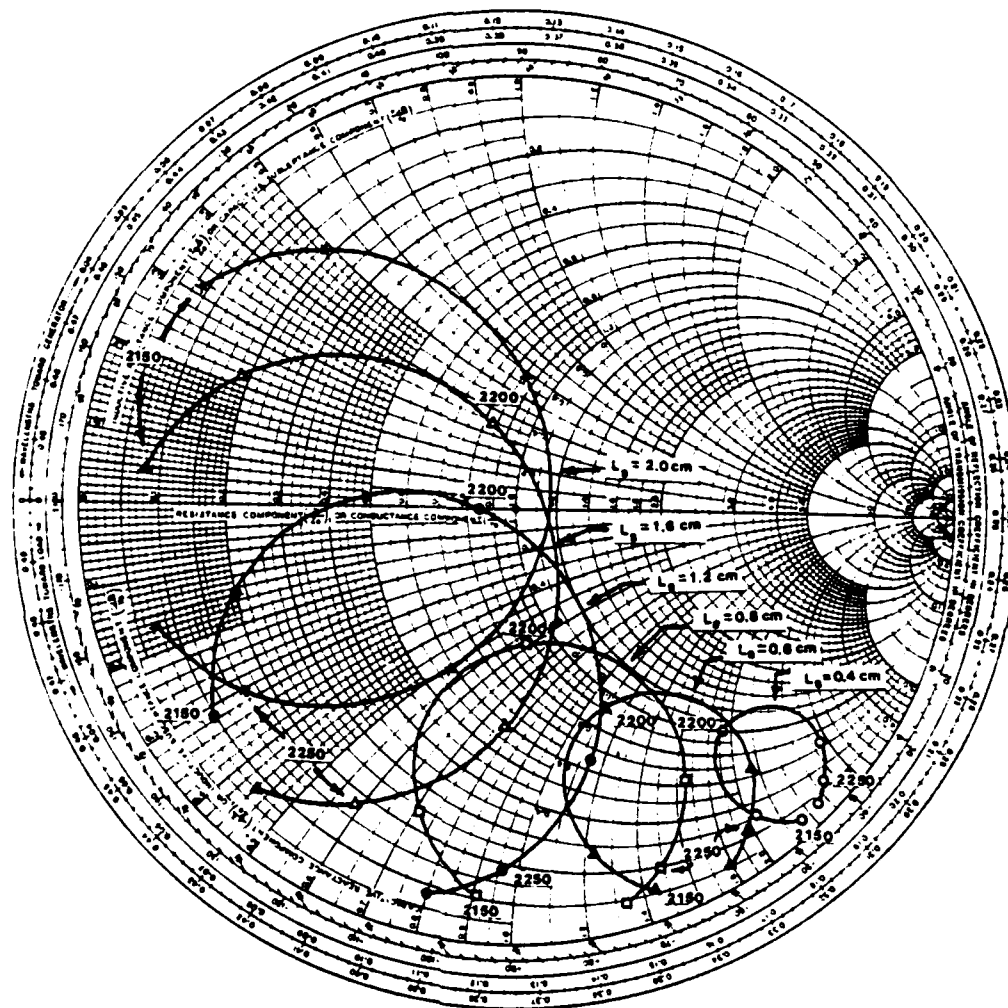


Figure 3.7 Measured input impedance loci as a function of stub length. (See figure 3.1 for antenna parameters.)

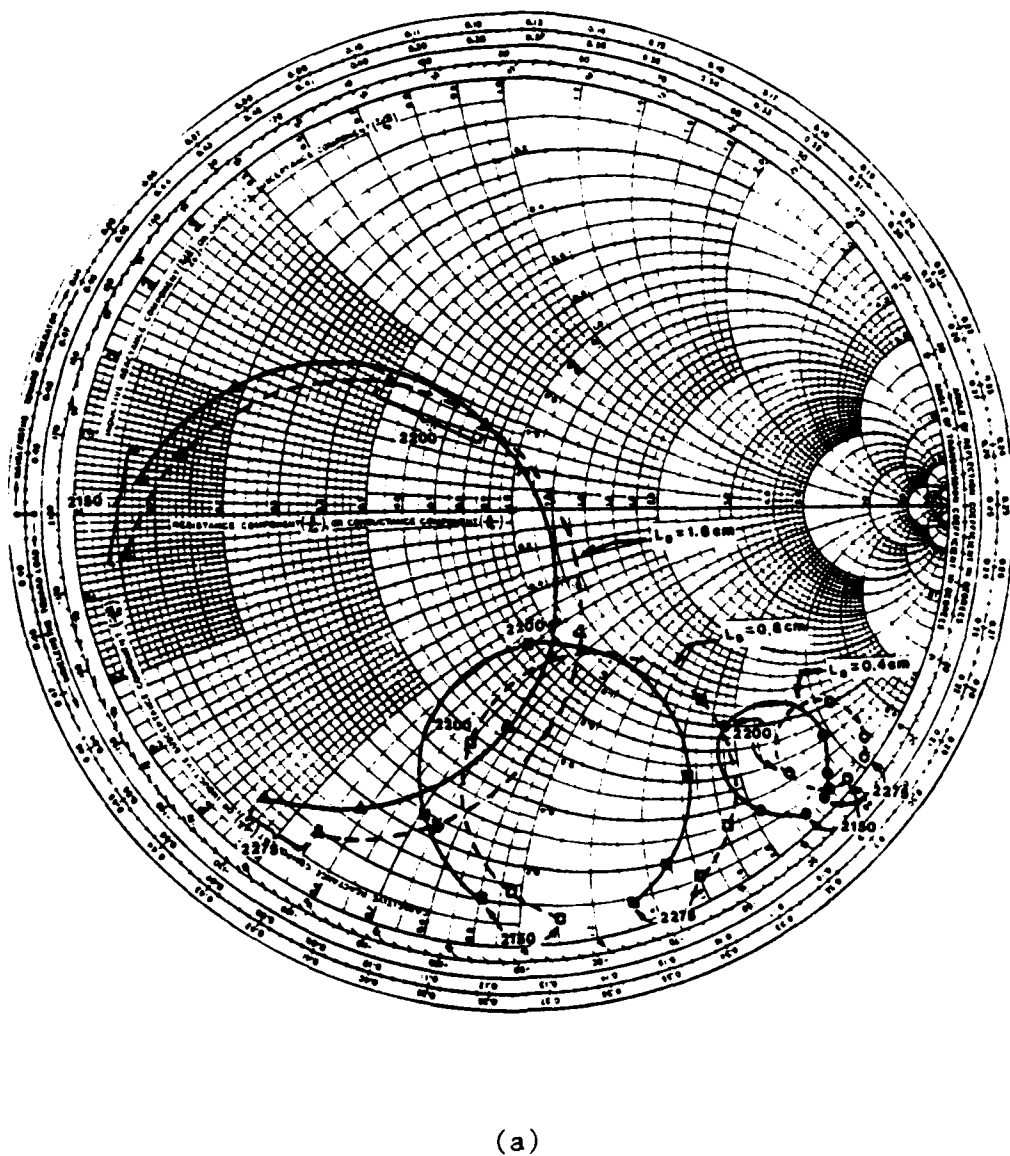
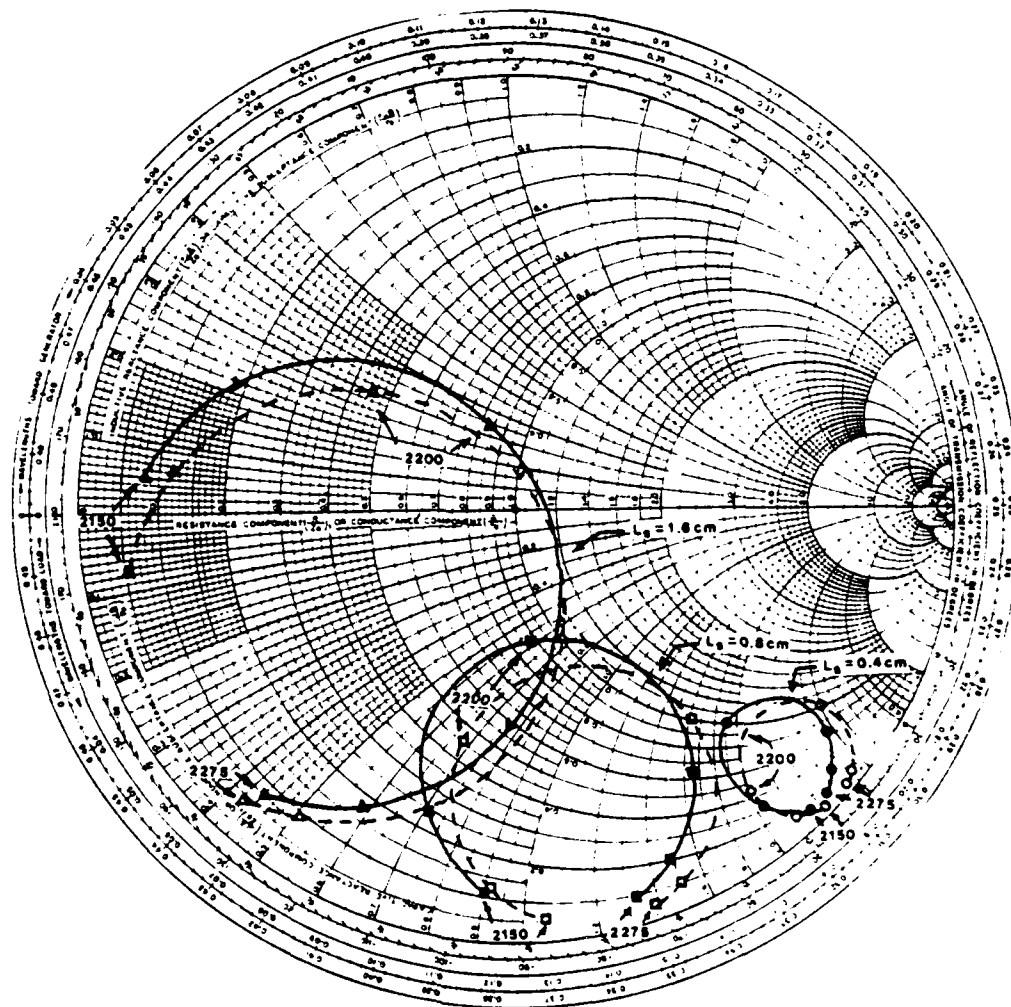


Figure 3.8 Measured versus calculated input impedance loci as a function of stub length. (See figure 3.1 for antenna parameters.)
 (a) Calculated points obtained with direct method.
 (b) Calculated points obtained with S-parameter method.



(b)

Figure 3.8 continued

series impedance, only the imaginary part of the input impedance at any frequency changes as the length of the open circuited stub varies.

A comparison of the above result with calculated loci is shown in Figure 3.8. Only every other curve of Figure 3.7 is shown in order to improve the clarity of the comparison. Input impedance data calculated by the direct method is displayed in Figure 3.8a, whereas the S-parameter method was used to produce the analytic impedance plots in Figure 3.8b. In both cases the analytic curves approximate the measured loci reasonably well.

Another empirical study conducted with the antenna of Figure 3.1 was to vary the patch position relative to the aperture. Measured and calculated plots are given in Figure 3.9 corresponding to movement of the patch in the \hat{y} -direction, i.e., along the resonant dimension (see Figure 2.2a). Calculated points utilizing the direct method and the S-parameter method are plotted in Figure 3.9a and 3.9b respectively. The agreement is good in both cases. The coupling factor, as defined by the radius of the resonance circle, is greatest when the patch is centered over the aperture and drops significantly as the patch is moved in the \hat{y} -direction. This is in accordance with Pozar's [1] simple model for this antenna based on Bethe hole theory and the cavity model. In addition, as the patch is offset in the \hat{y} -direction the centers of the resonant loops move approximately in a straight line towards the edge of the Smith chart just to the inductive side of the short position. This is probably due to the fact that when the patch is offset by a large

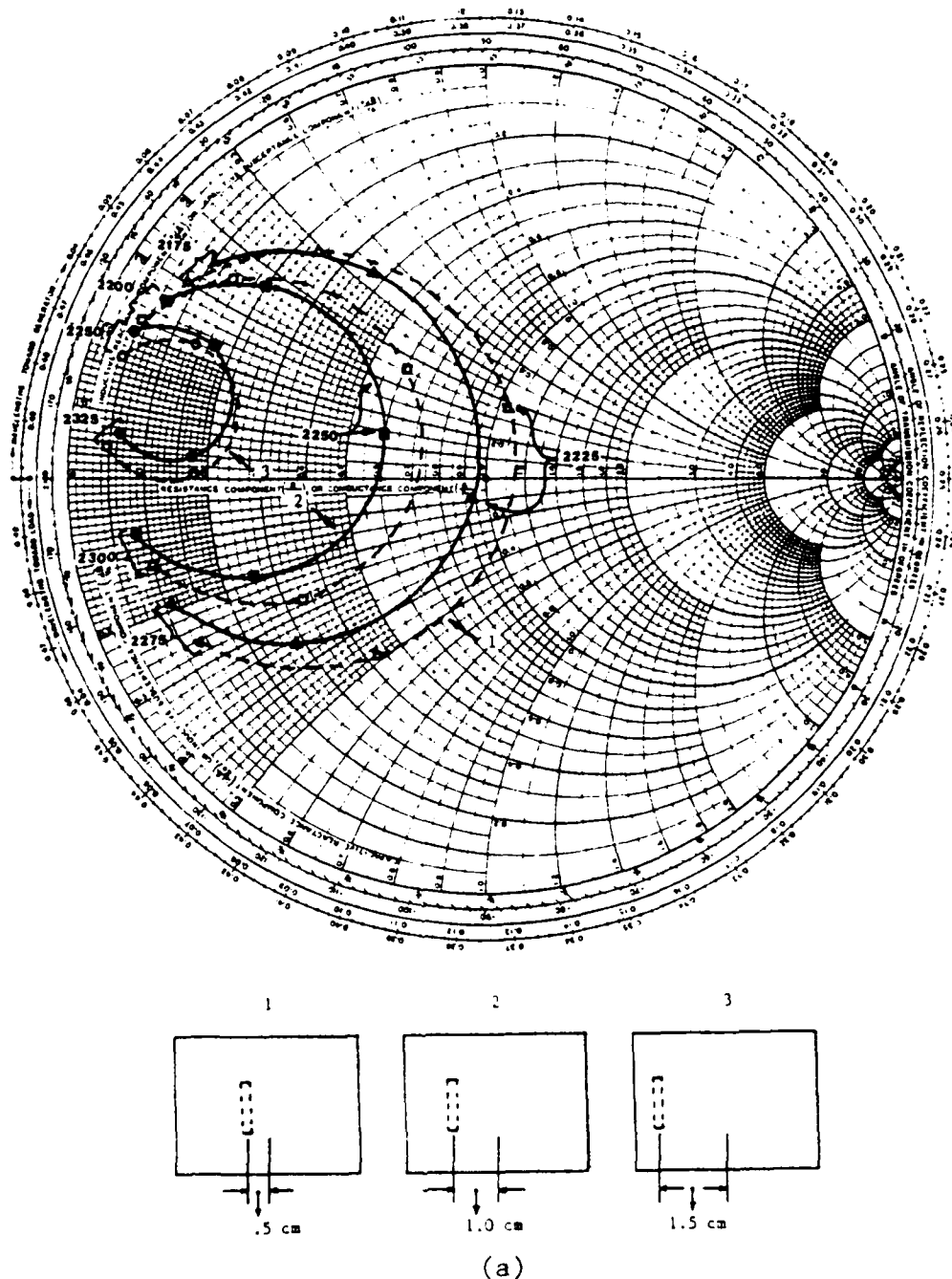


Figure 3.9 Measured versus calculated input impedance loci as a function of patch offset in the direction of resonance. The schematic above shows the relative position of the patch to the slot in each case. (See figure 3.1 for other antenna parameters.)

- (a) Calculated points obtained with direct method.
- (b) Calculated points obtained with S-parameter method.

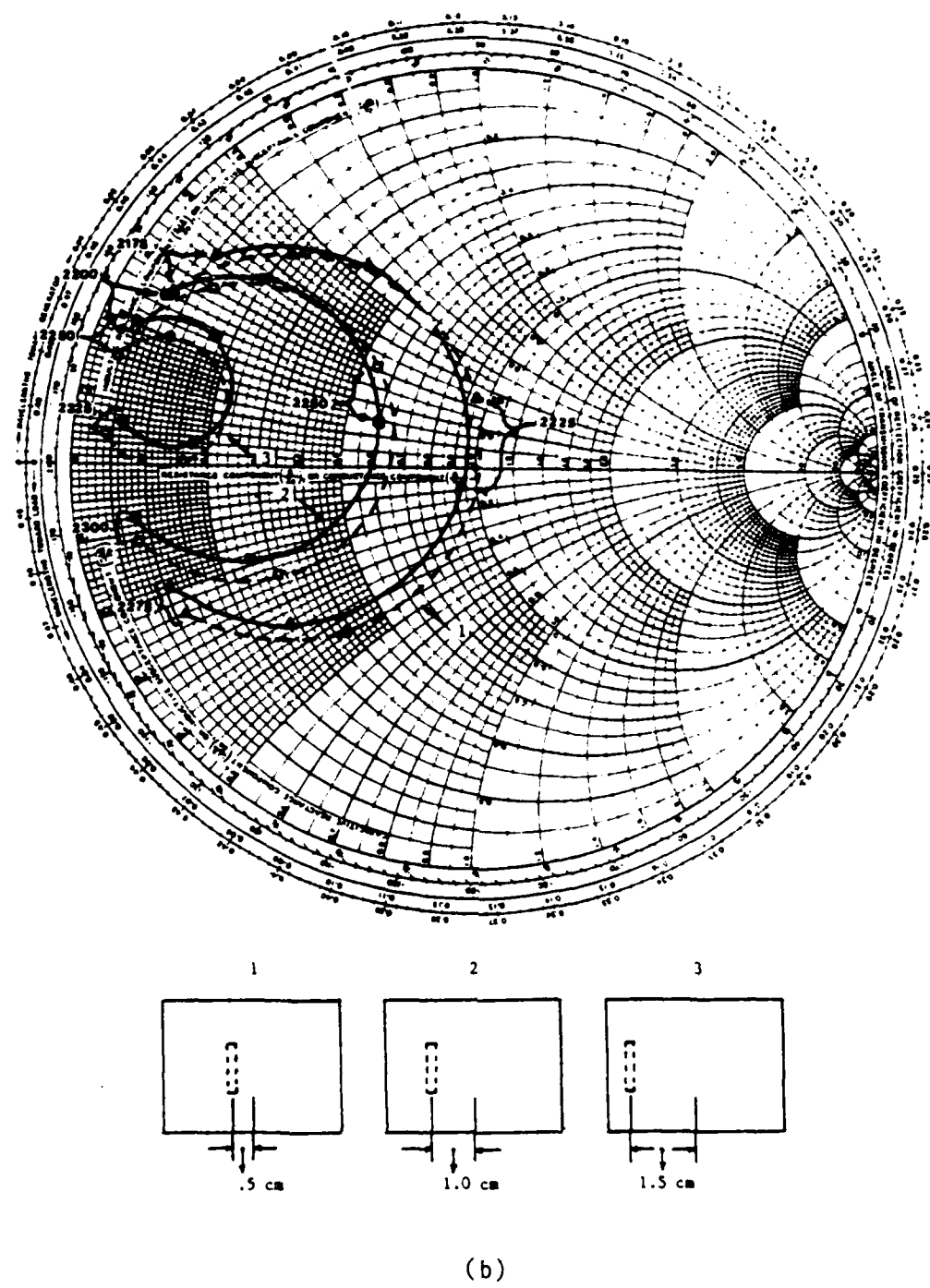


Figure 3.9 continued

amount the structure looks like a small aperture in a ground plane which is inductive.

In contrast to offsetting the patch in the \hat{y} -direction, lateral movement of the patch in the \hat{x} -direction causes little change in the coupling factor provided the entire slot remains under the patch. From the measured data in Figure 3.10 it can be seen that the coupling factor actually increases as the edge of the patch aligns with the edge of the slot and then monotonically decreases as the slot emerges from under the patch. Figure 3.11 shows calculated loci versus \hat{x} -offset of the patch. Initially the coupling factor remains constant, however at the point where the coupling factor increases empirically it decreases analytically. This causes a significant discrepancy between measured and calculated results for all large patch offsets in the \hat{x} -direction. This disagreement is not unexpected since our model utilizes only one mode in the aperture. A single aperture mode makes the analysis numerically more tractable but cannot account for skewing of the aperture electric field distribution as the patch is offset in a direction parallel to the long dimension of the slot. In addition, the patch current is assumed uniform in the \hat{x} -direction which may not be adequate for large offsets in that direction.

All subsequent parameter studies are based solely on analytic results. The direct method of calculating input impedance was selected rather than the S-parameter method for these studies because; (1) the agreement between the two methods is within the limits of measurement

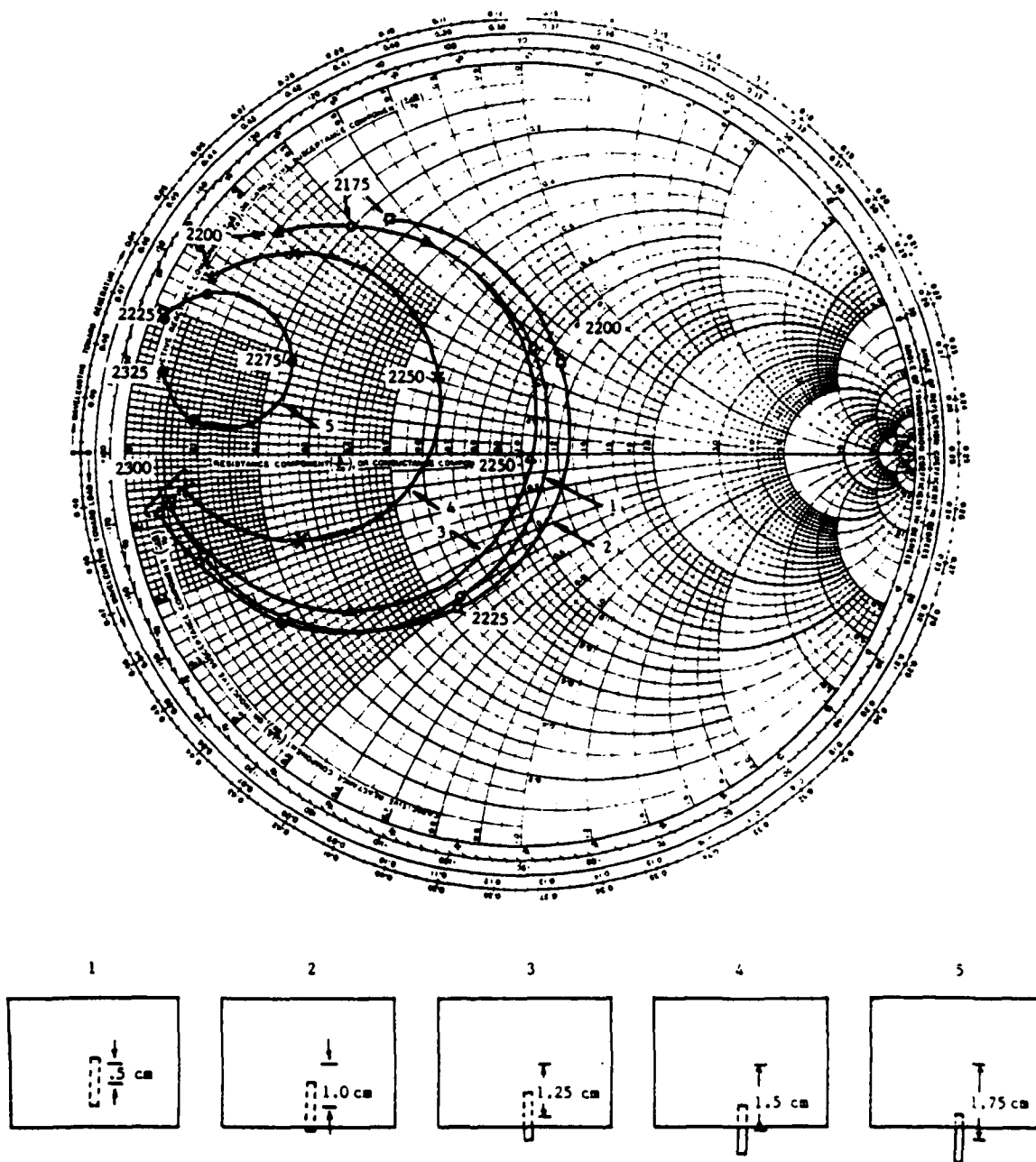


Figure 3.10 Measured input impedance loci as a function of patch offset in the direction orthogonal to resonance. The schematic shows the relative position of the patch to the slot in each case. (see figure 3.1 for other antenna parameters.)

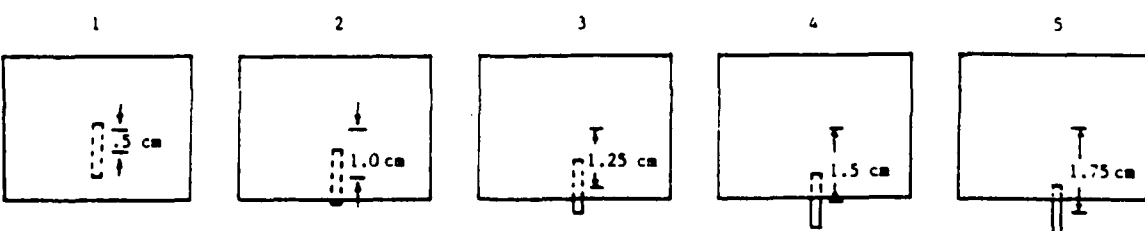
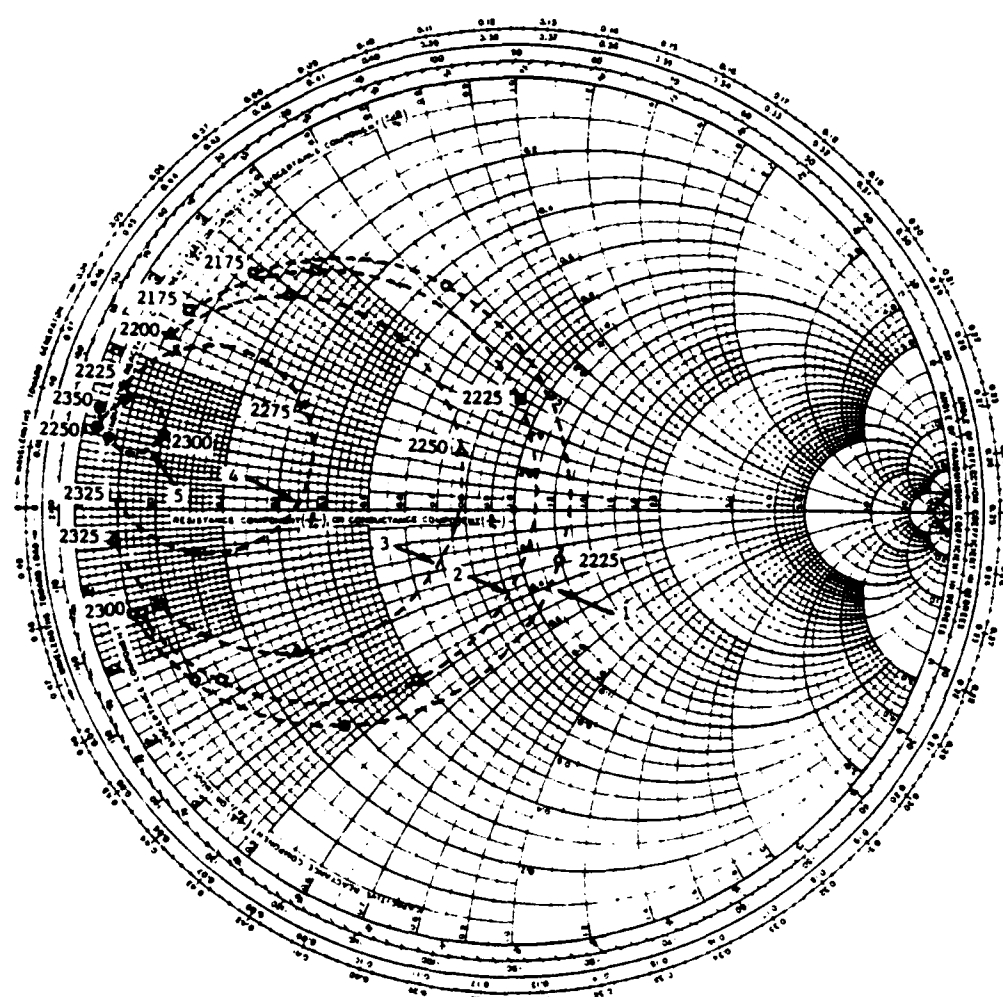


Figure 3.11 Calculated (direct method) input impedance loci as a function of patch offset in the direction orthogonal to resonance. The schematic shows the relative position of the patch to the slot in each case. (See figure 3.1 for other antenna parameters.)

accuracy, (2) the direct method is slightly faster except in the case of stub length variation studies, (3) all currents for the tuned antenna, i.e., feed line terminated in an open circuit, are obtained explicitly with the direct method as a function of the parameter varied.

The long dimension of the aperture was varied to obtain the curves given in Figure 3.12. The antenna dimensions are given in the Figure legend and are very similar to the dimensions of the antenna of Figure 3.1. As the aperture length is reduced the radius of the impedance circle decreases and the center of the circle moves towards the short circuit location. The resonant frequency versus aperture length is plotted in Figure 3.13. The resonant frequency, which in this case is also the minimum VSWR frequency, decreases with increasing slot length. Also plotted in Figure 3.13 is the input impedance at resonance versus slot length which can be used to approximately determine the slot length required to achieve critical coupling and the corresponding resonance frequency. In this case the aperture length which yields critical coupling is 1.09 cm at a resonant frequency of 2.233 GHz. For comparison the resonant frequency of this antenna based on the cavity model is 2.306 GHz [3].

It is also of interest to examine the influence of feed substrate dielectric constant and thickness on the input impedance, since the feed substrate will be electrically thick in the intended application of the antenna. As dielectric constant and thickness are varied in these studies the feed line width and stub length are modified to maintain a

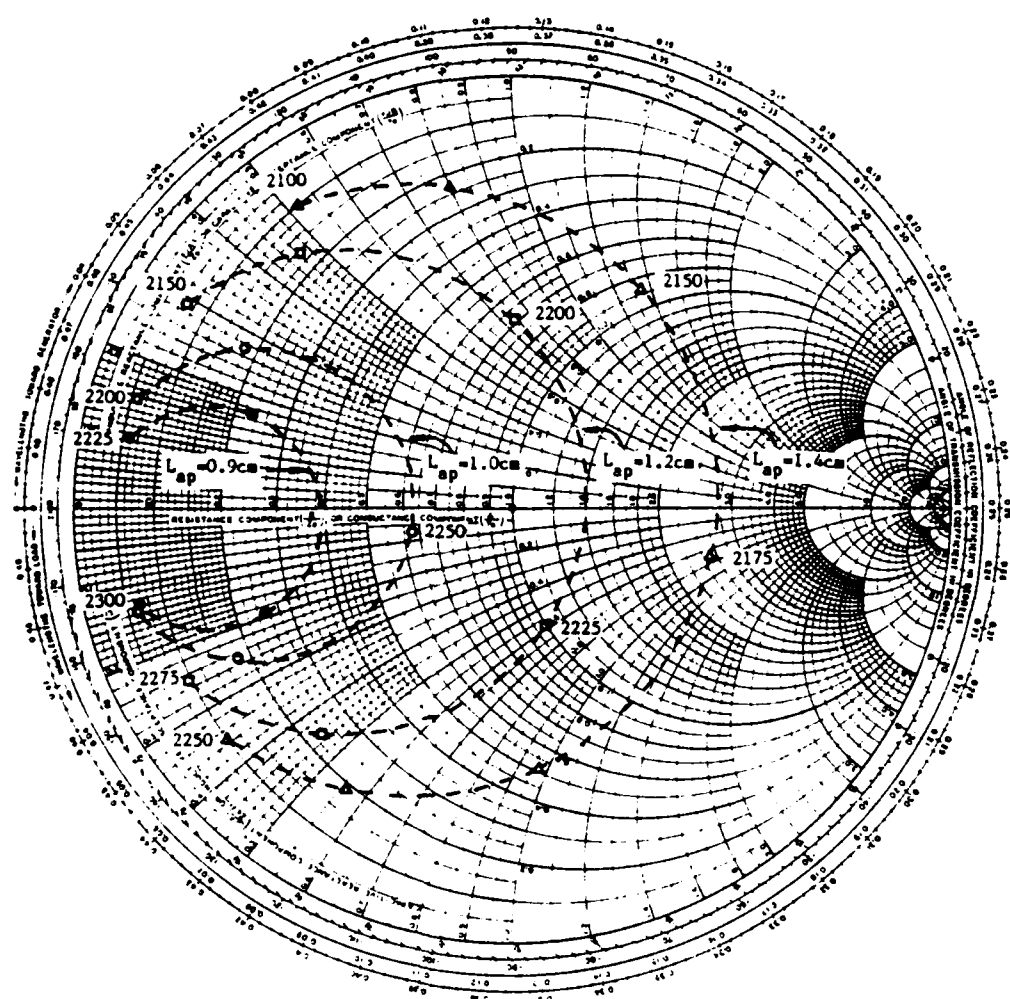


Figure 3.12 Calculated (direct method) input impedance loci as a function of aperture length (long dimension). The other antenna parameters are:

$\epsilon_r^b = 2.54$, $d_b = .16\text{cm}$, $L_p = 4.0\text{cm}$, $W_p = 3.0\text{cm}$, $x_{os} = 0.0\text{cm}$, $y_{os} = 0.0\text{cm}$,
 $W_{ap} = .11\text{cm}$, $\epsilon_r^a = 2.54$, $d_a = .16\text{cm}$, $W_f = .495\text{cm}$, $L_s = 2.0\text{cm}$

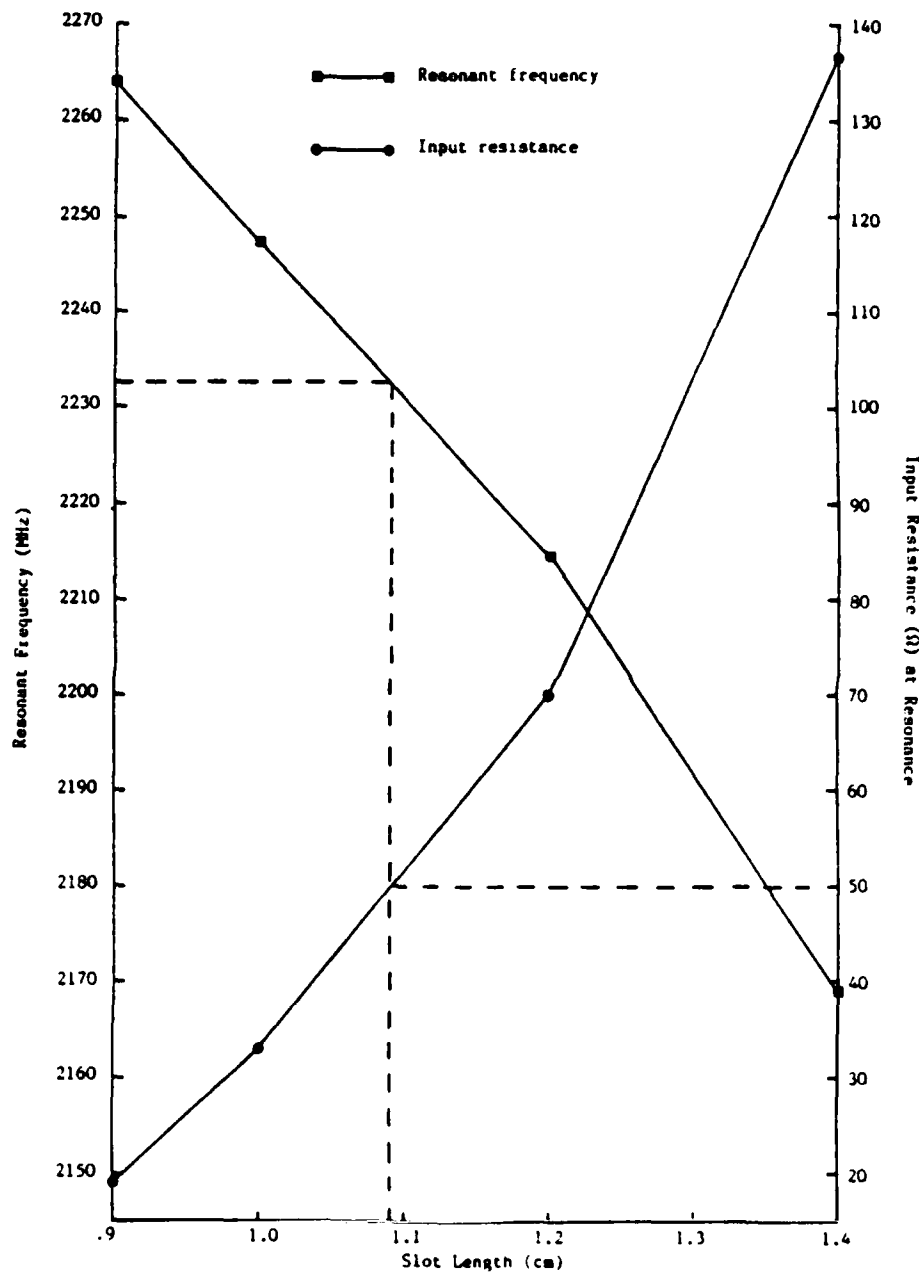
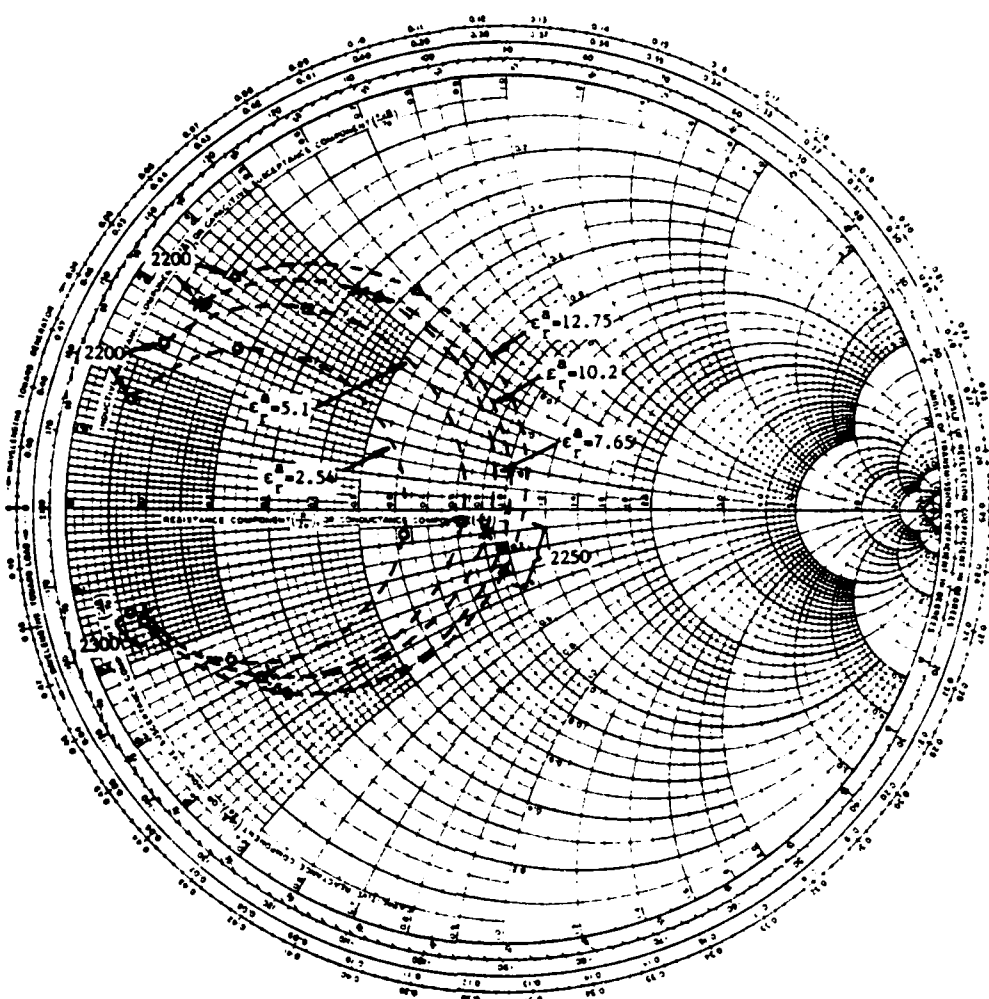


Figure 3.13 Resonant frequency and input resistance at resonance versus slot length (data from figure 3.12).

characteristic impedance of 50Ω and a stub length of $.22 \lambda_f$. All other antenna parameters were held constant and are given in the figure legends.

The dielectric constant variation is shown in Figure 3.14. The key features are the increase in the coupling factor and the invariance of the resonance frequency with increasing dielectric constant. The increase in the coupling factor is probably due to the fact that the electric length of the slot is increasing as the dielectric constant of the feed increases.

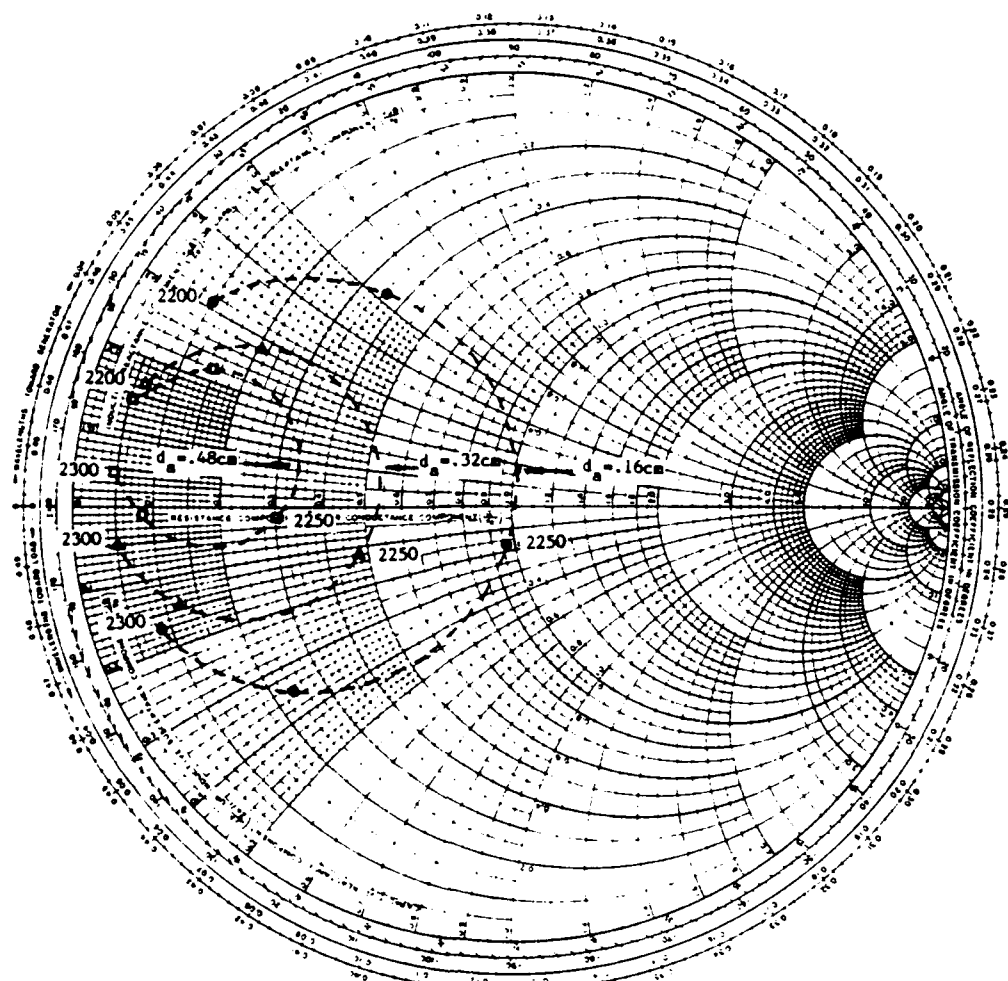
The last parameter study performed was to increase the thickness of the feed substrate of the antenna of Figure 3.14 in the case of $\epsilon_r = 10.2$. As the distance between the feedline and aperture increases, the coupling factor decreases as can be seen in Figure 3.15. As with the dielectric constant variations, the resonant frequency is unchanged with changes in substrate thickness over the range studied.



ϵ_r^a	W_f	L_s
2.54	.495 cm	2.000 cm
5.10	.310 cm	1.493 cm
7.65	.225 cm	1.255 cm
10.20	.173 cm	1.108 cm
12.75	.139 cm	1.004 cm

Figure 3.14 Calculated (direct method) input impedance loci as a function of feed substrate dielectric constant. The tabular data above gives the feed line width and stub length used in the analysis to maintain a 50Ω characteristic impedance and a stub length of $.22\lambda_f$ for each value of ϵ_r^a . The other antenna parameters are:

$\epsilon_r^b = 2.54$, $d_b = .16\text{cm}$, $L_p = 4.0\text{cm}$, $W_p = 3.0\text{cm}$, $x_{os} = 0.0\text{cm}$, $y_{os} = 0.0\text{cm}$,
 $L_{ap} = 1.0\text{cm}$, $W_{ap} = .11\text{cm}$, $d_a = .16\text{cm}$.



d_a	W_f	L_s
.16 cm	.173 cm	1.108 cm
.32 cm	.375 cm	1.083 cm
.48 cm	.613 cm	1.056 cm

Figure 3.15 Calculated (direct method) input impedance loci as a function of feed substrate thickness. The tabular data above gives the feed line width and stub length used in the analysis to maintain a 50Ω characteristic impedance and a stub length of $.22\lambda_f$ for each value of d_a . The other antenna parameters are:

$\epsilon_r^b = 2.54$, $d_b = .16\text{cm}$, $L_p = 4.0\text{cm}$, $W_p = 3.0\text{cm}$, $x_{os} = 0.0\text{cm}$, $y_{os} = 0.0\text{cm}$,
 $L_{ap} = 1.0\text{cm}$, $W_{ap} = .11\text{cm}$, $\epsilon_r^a = 10.2$.

CHAPTER IV

CONCLUSION

A rectangular microstrip antenna coupled to a microstrip line through a small rectangular aperture in the ground plane has been analyzed by the moment method. In the case of a feed line terminated in an open circuit the input impedance is determined from the amplitude coefficient of a reflected traveling wave current mode on the feed line. In the case of an infinite feed line the S-parameters are calculated by including both reflected and traveling wave current modes on the feed line. These amplitude coefficients are obtained directly from the moment method solution.

The analysis has been verified by comparison with measured input impedance data for an antenna with a low dielectric constant ($\epsilon_r = 2.54$) feed substrate and one with a high dielectric constant ($\epsilon_r = 10.2$) feed substrate. In the former case empirical parameter studies, which involved varying the length of the feed line beyond the aperture and lateral displacements of the antenna with respect to the aperture, were carried out and compared with analytical studies to further validate the theory. With the exception of patch offsets orthogonal to the resonant dimension of the patch the analytical and empirical results were in good agreement. From the above data and S-parameter results an equivalent two-port lumped element circuit is proposed for the aperture backed by a

microstrip antenna near resonance. The circuit is a series impedance consisting of a parallel RLC circuit in series with an inductor. Finally, analytical parameter studies have been performed to determine the effect of aperture length and feed substrate dielectric constant and thickness on input impedance and resonant frequency.

Further development of the proposed equivalent circuit for this antenna should be undertaken in the future. The circuit elements could be found by determining the stub length that yields an admittance locus which follows a constant conductance circle. The series reactance due to L' would then be the negative of the reactance looking into the open circuited stub, from which L' could be determined. The resistance, R , of the model would simply be the inverse of the input conductance (constant under the condition stated above) near resonance and L and C could be determined from the input susceptance at two frequencies around resonance. By performing parameter studies and examining the effect on the equivalent circuit element values, the antenna parameters which most strongly influence each circuit element might be elucidated. Another area for future work is to determine the far-field antenna patterns from the currents on the patch, aperture and feed line. Of particular interest would be the relative magnitude of the lobe on the feed side versus that on the antenna side. Finally, improved programming techniques should be sought to reduce the CPU time required to carry out the analysis. Most importantly, this would make it feasible to expand the aperture magnetic current in more than one basis mode.

REFERENCES

- [1] Pozar, D. M., "Microstrip antenna aperture-coupled to a microstripline," Electronics Letters, vol. 21, no. 2, pp. 49-50, Jan. 1985.
- [2] Schaubert, D. H., K. S. Yngvesson, D. M. Pozar and R. W. Jackson, "Technology development for monolithic millimeter wave phased arrays," Quarterly Progress Report, Project No. F19628-84-k-0022, Univ. of Massachusetts, Dept. of Elec. and Comp. Eng., July, 1984.
- [3] Carver, K. R. and J. W. Mink, "Microstrip antenna technology," IEEE Trans. Antennas Propagat., vol. AP-29, pp. 2-24, Jan. 1981.
- [4] Jackson R. W. and D. M. Pozar, "Full-wave analysis of microstrip open-end and gap discontinuities", To appear in IEEE Trans. Microwave Theory Tech., issue on numerical methods, Oct. 1985
- [5] Harrington, R. F.: "Time Harmonic Electromagnetic Fields," McGraw-Hill book Company, New York, 1961.
- [6] Pozar D. M., "Input impedance and mutual coupling of rectangular microstrip antennas," IEEE Trans. Antennas Propagat., vol. AP-30, no. 6, pp. 1191-1196, Nov. 1985.

MISSION
of
Rome Air Development Center

RADC plans and executes research, development, test and selected acquisition programs in support of Command, Control Communications and Intelligence (C³I) activities. Technical and engineering support within areas of technical competence is provided to ESD Program Offices (POs) and other ESD elements. The principal technical mission areas are communications, electromagnetic guidance and control, surveillance of ground and aerospace objects, intelligence data collection and handling, information system technology, solid state sciences, electromagnetics and electronic reliability, maintainability and compatibility.

DTIC
FILMED

4-86

END